Simulation of absorbing aerosol indices for African dust

Masaru Yoshioka[1,2,3] and Natalie Mahowald[1,2,3]
Bren School of Environmental Science and Management, University of California, Santa Barbara, California, USA

Jean-Louis Dufresne[4]
Laboratoire de Météorologie Dynamique, Institut Pierre Simon Laplace, CNRS, Paris, France

Chao Luo[1,2,5]
Bren School of Environmental Science and Management, University of California, Santa Barbara, California, USA

[1]   It has been speculated that the vegetation change and human land use have modulated the dust sources in North Africa and contributed to the observed increase of desert dust since 1960s. However, the roles of surface disturbances on dust generation are not well constrained because of limitations in the available data and models. This study addresses this issue by simulating the Total Ozone Mapping Spectrometer (TOMS) Absorbing Aerosol Indices (AAIs) for model-predicted dust and comparing them with the observations. Model simulations are conducted for natural topographic depression sources with and without adding sources due to vegetation change and cultivation over North Africa. The simulated AAIs capture the previously reported properties of TOMS AAI as well as observed magnitude and spatial distribution reasonably well, although there are some important disagreements with observations. Statistical analyses of spatial and temporal patterns of simulated AAI suggest that simulations using only the natural topographic source capture the observed patterns better than those using 50% of surface disturbance sources. The AAI gradients between Sahara (north) and Sahel (south) suggest that the best mixture of surface disturbance sources is 20–25%, while spatial and temporal correlations suggest that the optimum mixture is 0–15% with the upper bound of 25–40%. However, sensitivity studies show that uncertainties associated with meteorology and source parameterization are large and may undermine the findings derived from the simulations. Additional uncertainties will arise because of model errors in sources, transport, and deposition. Such uncertainties in the model simulations need to be reduced in order to constrain the roles of different types of dust sources better using AAI simulation.

Citation: Yoshioka, M., N. Mahowald, J.-L. Dufresne, and C. Luo (2005), Simulation of absorbing aerosol indices for African dust, *J. Geophys. Res.*, *110*, D18S17, doi:10.1029/2004JD005276.

1. Introduction

[2]   Dust from the arid regions of North Africa is transported long distances and modifies the atmospheric radiative budget [e.g., *Miller and Tegen*, 1998] as well as biogeochemistry at a regional scale [e.g., *Chadwick et al.*, 1999; *Martin*, 1990]. However, current estimates of anthropogenic impacts of mineral aerosols have large uncertainties [*Intergovernmental Panel on Climate Change*, 2001]. These large uncertainties are a product of uncertainties at microscopic and macroscopic levels; the former includes mineralogy, size distribution, particle shapes, and state of mixing with other species, and the latter includes spatiotemporal distribution and the anthropogenic portion of dust.

[3]   Atmospheric desert dust generated by disturbances to the land surfaces such as the Sahel drought and anthropogenic land use change may represent an important part of the present mineral dust from North Africa and may have contributed to the observed large increase at Barbados [*Prospero and Nees*, 1986; *Tegen and Fung*, 1995; *Mahowald et al.*, 2002]. However, *Prospero et al.* [2002] argue that natural dry topographic depressions are the dominant sources of mineral dust aerosol through analyses of Total Ozone Mapping Spectrometer (TOMS) Absorbing Aerosol Index (AAI) data [*Herman et al.*, 1997; *Torres et al.*, 1998]. *Mahowald et al.* [2002] compare model simulations

---

[1]Also at Institute of Computational Earth System Science, University of California, Santa Barbara, California, USA.
[2]Also at Climate and Global Dynamics Division, National Center for Atmospheric Research, Boulder, Colorado, USA.
[3]Now at Climate and Global Dynamics Division, National Center for Atmospheric Research, Boulder, Colorado, USA.
[4]Formerly at Institute of Computational Earth System Science, University of California, Santa Barbara, California, USA.
[5]Now at Earth System Science, University of California, Irvine, California, USA.

of dust mobilized from natural topographic depressions and disturbed sources and show that they cannot be distinguished over North Africa by TOMS-derived aerosol optical depths (AODs) [*Torres et al.*, 2002] or other available data. *Luo et al.* [2003] extended this study and showed that differences in model simulations due to meteorology or source parameterizations are more important than differences due to different sources. Recently, *Tegen et al.* [2004] estimated by using dust storm frequency that the land use source accounts for <10% of the global dust load, while *Mahowald et al.* [2004] using the same data show that 0–50% land use source is statistically indistinguishable using a different model and methodology.

[4] TOMS AAI is useful for observing absorbing aerosols such as black carbon and soil dust since it detects these aerosols over desert and vegetated land as well as over ocean [*Herman et al.*, 1997; *Torres et al.*, 1998]. However, as previously reported [*Herman et al.*, 1997; *Torres et al.*, 1998; *Hsu et al.*, 1999; *Mahowald and Dufresne*, 2004] and demonstrated in section 3 of this paper, the value of TOMS AAI depends on vertical profile of an aerosol in addition to its column loading, size distribution and optical properties. This characteristic has complicated the use of TOMS AAI in its interpretation and application for diagnosis of model simulated aerosols. For example, identification of source regions of desert dust using TOMS AAI [e.g., *Goudie and Middleton*, 2001; *Prospero et al.*, 2002] may be sensitive to the actual height of dust aerosol. Attempts to compare TOMS AAI against model-derived AOD [e.g., *Zender et al.*, 2003a; *Mahowald et al.*, 2003] have been hampered by the nonunique relationship between AAI and AOD. Estimates of AOD from TOMS AAI such as done by *Torres et al.* [2002] rely on dust height prescribed by model and thus no longer are model-independent quantities.

[5] In this study, as an alternative way to utilize TOMS AAI and compare model simulations and observations, we estimate TOMS AAI over North Africa by simulating the radiances that the TOMS sensor would measure if dust were present in the atmosphere as predicted by the model. Since a three-dimensional (3-D) atmospheric transport model provides estimate of vertical profile, column loading and size distribution of aerosol all together, this method determines AAI uniquely for an assumed optical property and a model simulated aerosol distribution without assuming any of these parameters. Note that the 3-D aerosol distribution is self-consistent as contrasted to the case of AOD estimated from TOMS AAI in which the height of aerosol is, in general, prescribed with a different model from the one to be diagnosed. Bias in the model simulated AAI may be a product of errors in the model used to simulate dust and exogenously given optical properties but not an error in other model. However, whether the bias in the simulation is due to the column loading, the vertical profile, size distribution, or assumed optical property of dust is not generally clear. In this study, biases in simulated AAI are mainly attributed to the bias of dust loading in order to derive the spatial and temporal distribution of dust source while considering other possibilities as well by analyzing the simulations.

[6] Similar methods are used in recently published papers. *Ginoux and Torres* [2003] derived empirical function of TOMS AAI with surface pressure, single scattering

albedo, optical depth and height of aerosol layer and proposed applications of this method in validating simulated dust distributions and in characterizing dust source areas. Their daily empirical aerosol indices (AIs) correlate moderately (correlation coefficients are between 0.3 and 0.6) and monthly mean AI's correlate well (between 0.6 and 0.9) with TOMS AAI over dust source regions in North Africa. *Ginoux et al.* [2004] calculated AAI using model-predicted dust and radiative transfer calculation. This is basically the same method as in this paper, and the differences are briefly summarized in section 2.3. AIs are calculated over North Africa and North Atlantic with these two methods for the same model simulated dust field. They are shown to agree well with each other and be capable to capture the magnitude and distribution of a specific dust plume observed in TOMS AAI quite well.

[7] We conduct systematic comparisons between TOMS and model simulated AAIs over North Africa over the period of 1984 to 1990, during which TOMS measurements were most stable [*Cakmur et al.*, 2001; *Torres et al.*, 2002; R. D. McPeters et al., Nimbus 7 Total Ozone Mapping Spectrometers (TOMS) data products user's guide, 1996, available at http://toms.gsfc.nasa.gov/datainfo/n7usrguide.pdf, hereinafter referred to as McPeters et al., TOMS user's guide, 1996]. Our goal is to constrain the role of disturbances on the land surface in modulating dust sources, and thus we include natural topographic depression sources, disturbed vegetation sources and land use sources. We conduct several sensitivity studies to determine how important other factors are in producing uncertainties and biases in our results.

[8] In section 2, models, schemes, data and methods used in this study are described. Section 3 shows general features of the base case simulations that will help basic understanding of AAI simulations. Section 4 presents sensitivity studies to assess the errors due to assumptions used to calculate monthly mean AAIs throughout this study in comparison to calculations under more realistic conditions with these assumptions relaxed. Section 5 investigates the roles of different source processes through statistically analyzing how well the simulations reproduce the observed patterns. Sensitivity studies using different meteorological data sets and mobilization schemes are conducted in section 6 in order to further investigate the biases in simulations seen in section 5 and evaluate uncertainties involved in the simulations. Section 7 integrates the results and analyses from previous sections and discusses the biases in the simulations and the roles of different source processes. Finally, section 8 concludes the study.

2. Methods
2.1. Dust Mobilization, Transport, and Deposition

[9] Model simulations described in detail by *Mahowald et al.* [2002], *Luo et al.* [2003] and *Mahowald et al.* [2003] as well as several new sensitivity studies described below are used in this study. In the main part of this study, the Model of Atmospheric Transport and Chemistry (MATCH) [*Rasch et al.*, 1997; *Mahowald et al.*, 1997] is coupled with Dust Entrainment and Deposition (DEAD) model [*Zender et al.*, 2003b] to simulate dust mobilization (entrainment), transport, and deposition. National Center for Environmen-

tal Prediction/National Center for Atmospheric Research (NCEP) reanalysis data [Kalnay et al., 1996; Kistler et al., 2001] are used to drive the coupled model at the T62 resolution ($1.8° \times 1.8°$) and with 28 vertical levels. For comparison, the MATCH transport model is also coupled with the Georgia Tech/Goddard Global Ozone Chemistry Aerosol Radiation and Transport (GOCART) mobilization scheme [Ginoux et al., 2001; Luo et al., 2003] and driven by the meteorological data set of the National Aeronautics and Space Administration Data Assimilation Office (NASA DAO) for 1995. Simulations using DAO data are conducted at the same horizontal resolution but with 20 vertical levels.

[10] The DEAD mobilization scheme is based on the friction velocity (wind stress at the surface), which is a function of the wind speed, roughness length and the atmospheric stability at the surface. The mass flux of saltating particles depends on the excess of the wind friction speed over the threshold wind friction velocity for saltation. The saltating particle flux F_h was calculated by White's [1979] formulation:

$$F_h = c \frac{\rho_a}{g} U^{*3} \left(1 - \frac{U_t^{*2}}{U^{*2}} \right)$$

where c is constant, ρ_a is the atmospheric density, U^* is the wind friction speed, g is acceleration of gravity, and U_t^* is the threshold wind friction speed. The threshold velocity is calculated by a semiempirical parameterization as a function of particle density and diameter and air density [Iversen and White, 1982], and modified for soil moisture following Fecan et al. [1999]. We use the relation between the vertical and horizontal flux from Marticorena and Bergametti [1995]

$$\log(F_v/F_h) = 0.134(\% \text{ clay}) - 6$$

and globally uniform value of clay fraction of 20%. The mobilization is sensitive to wind velocity, atmospheric stability and soil wetness.

[11] The dust mobilization in GOCART model is based on empirical formulation by Gillette and Passi [1988]:

$$F_p = CSs_p U_{10 \text{ m}}^2 (U_{10 \text{ m}} - U_t) \qquad U_{10 \text{ m}} > U_t$$

$$F_p = 0 \qquad\qquad\qquad \text{otherwise}$$

where C is a dimensional factor, S is source function, $U_{10 \text{ m}}$ is the horizontal wind speed at 10 m, U_t is the threshold velocity, and s_p is the fraction of each of seven size classes. The threshold velocity depends on the particle size and soil moisture. The threshold velocity was calculated with modified Belly's [1964] relationship as a function of surface wetness, particle diameter and density, and air density [Ginoux et al., 2001].

[12] We use four aerosol size bins with the diameter ranges of 0.1–1.0, 1–2.5, 2.5–5.0, and 5.0–10.0 μm and assume a lognormal size distribution within each size bin [Zender et al., 2003b]. Because of the uncertainties in the available soil texture data, we assume globally uniform mass fractions in each bin at source to be 0.1, 0.3, 0.3, and 0.3. (These mass fractions are the same as Tegen and Fung [1994] and Ginoux et al. [2001], although our size

ranges are different from theirs so that we have more mass in smaller size ranges. The sensitivity of assuming different size distribution is examined in section 4.5.) The resulting diurnal mean global dust distributions are averaged over each month for the region of 10.5°N–39.0°N; 30.0°W–30.0°E, which includes North Africa and eastern North Atlantic but excludes low-latitude regions where biomass burning aerosol (which is also detected by TOMS AAI) is abundant. Since this does not guarantee the domain is free from biomass burning aerosols and especially the southern part of the domain may be prone to contamination of biomass burning aerosols, however, an additional analysis is conducted excluding winter months when biomass burning is active in section 5.4. The dust concentrations in the simulations have been made smaller by 8% relative to the globally tuned values in previous studies [Luo et al., 2003; Mahowald et al., 2002] in order to match the TOMS AAI over this region.

2.2. Source Regions

[13] Dry, unvegetated topographic depressions are considered as dust sources due to the input of fine soil particles [Prospero et al., 2002; Ginoux et al., 2001] and used in our base case (B) simulations. In order to explore the role of surface disturbance, we look at "new desert (D)" and "cultivation (C)" source regions [Mahowald et al., 2002]. New desert regions are defined as "potential source areas" or dry and unvegetated areas in 1980–1984 but not in 1965–1969 using the BIOME3 equilibrium vegetation model [Haxeltine and Prentice, 1996] (driven by precipitation from Dai et al. [1996] and temperature and cloudiness from NCEP reanalysis). New desert areas previously supported plants, which acted to hold down the soils. When the plants are removed, there should be larger amounts of easily erodible soils than in regions that have long been desert, similar to the "Sahara Boundary Shift" source by Tegen and Fung [1995]. Cultivation source regions have dry, unvegetated soils being cultivated or used for pasture and are defined using the Matthews [1983] data set when there is a desert as defined by the BIOME3 equilibrium vegetation model. We are presuming that the land use would disturb the soils and allow the soil particles to be more easily mobilized [e.g., Saxton et al., 2000]. Therefore the sizes and locations of new desert source and cultivation source, shown by Mahowald et al. [2002, Figure 3], are sensitive to any bias in BIOME3 model simulations. These sources are used in combination with the topographic depression sources in simulations (cases BD and BC) so that each type of source accounts for 50% of the total dust mobilized in North Africa. We also isolate the topographic depression source in Lake Chad/Bodele Depression area for further sensitivity studies (case BL), where the source in this area is four times larger than in the original simulations and accounts for 15% of total mobilization. Dust mobilization from North Africa west of 40°E is tuned to be equal in all these comparisons. Hereafter, BD, BC, and BL sources are collectively referred to as "combination sources."

2.3. Simulation of TOMS AAI

[14] The presence of ultraviolet (UV) absorbing aerosol is detected as AAI derived from TOMS measurements using a spectral contrast method in the near UV region where the

ozone absorption is very small [*Herman et al.*, 1997; *Torres et al.*, 1998]. In cloud-free conditions, AAI depends on the amount, size distribution, optical properties and height of absorbing aerosols, the solar and viewing geometries [*Herman et al.*, 1997; *Torres et al.*, 1998]. Here we estimate a Nimbus 7 TOMS AAI by simulating the TOMS measurements at two near UV bands through radiative transfer calculations for a dust profile and atmospheric and surface conditions given by the model.

[15] AAI is defined as [*Herman et al.*, 1997]

$$AAI = -100 * \left[\log_{10} \left(\frac{I_{dst;Rs}(340)}{I_{dst;Rs}(380)} \right) - \log_{10} \left(\frac{I_{clr;Rm}(340)}{I_{clr;Rm}(380)} \right) \right]$$

where $I_{dst;RAS}$ are radiance at 340 and 380 nm at the top of the atmosphere in presence of dust and surface reflectivity Rs, which would be measured by TOMS sensor in the real atmosphere and are to be simulated here. $I_{clr;Rm}$ are radiance that would be measured in absence of aerosols and calculated as follows [*Dave*, 1978; R. D. McPeters et al., TOMS user's guide, 1996]:

$$I_{clr;Rm} = I_{clr;Rs=0} + \frac{R_m * T}{1 - S * R_m}$$

The radiance $I_{clr;Rs=0}$ is computed assuming no aerosols and no reflection at the surface. The reflectivity R_m is assumed to be independent of wavelength and is calculated using radiances at 380 nm:

$$R_m = R_m(380) = \left[S(380) + \frac{T(380)}{I_{dst;Rs}(380) - I_{clr;Rs=0}(380)} \right]^{-1}$$

and T and S are transmission and atmospheric diffuse reflectivity, respectively, and given

$$T = \left(I_{clr;Rs=1} - I_{clr;Rs=0} \right) \frac{F_{clr;Rs=0}^{\downarrow sfc}}{F_{clr;Rs=1}^{\uparrow sfc}}$$

$$S = 1 - \frac{F_{clr;Rs=0}^{\downarrow sfc}}{F_{clr;Rs=1}^{\uparrow sfc}}$$

$F_{clr;Rs=0}^{\downarrow sfc}$ and $F_{clr;Rs=1}^{\uparrow sfc}$ are downward and upward surface irradiance for the clear sky with surface reflectivity of 0 and 1, respectively.

[16] We use the Santa Barbara DISORT Atmospheric Radiative Transfer (SBDART) model [*Ricchiazzi et al.*, 1998] to calculate the radiance and irradiance needed in the AAI calculation above. It incorporates the LOWTRAN7 band models [*Pierluissi and Peng*, 1985] and the DISORT discrete ordinate method [*Stamnes et al.*, 1988]. Therefore the simulated AAI is also called as MATCH-SBDART or MS AAI as contrasted to TOMS AAI. The optical properties are obtained through Mie calculations using model estimated particle size distributions and refractive indices from *Sinyuk et al.* [2003] and O. Torres (personal communication, 2003). The resulting single scattering albedoes at 380 nm for the four size bins are 0.948, 0.883, 0.851, are 0.861, respectively. Our computations reproduce the pub-

lished results of *Torres et al.* [1998] if the optical properties from that study are used. We use solar zenith angle calculated for each month and latitude at local solar noon since Nimbus 7 satellite has a Sun-synchronous orbit with a noon equator crossing time (McPeters et al., TOMS user's guide, 1996). The viewing angle is assumed to be nadir.

[17] *Ginoux et al.* [2004] use very similar method to this, in which they simulate radiance and flux using a radiative transfer model to calculate AAI. There are a few differences between our method and theirs. They use mass-weighted average altitude of dust while we use the whole vertical profile of dust predicted by the model. They calculate daily AAI using realistic satellite viewing angles, which is not done in this study because we calculate AAI for monthly averaged data. The effects of using monthly averaged dust and atmospheric variables and fixed viewing angle at nadir are evaluated in section 4. They use optical properties of dust in their seven size bins calculated through Mie theory using refractive index from *Colarco et al.* [2002]. Their method resolves optical properties in smaller sizes better and leads to higher absorption in larger particles (our single scattering albedo in $5.0-10.0$ μm diameter range is 0.861 and their value in $6.0-12.0$ μm range is 0.725 [see *Ginoux et al.*, 2004, Table 6]).

2.4. Comparisons With TOMS AAI Observations

[18] We calculate AAI for monthly averaged model-predicted dust distribution and compare with monthly average of Nimbus 7 TOMS AAI data over the period from 1984 to 1990, during which TOMS measurements were most stable [*Cakmur et al.*, 2001; *Torres et al.*, 2002; McPeters et al., TOMS user's guide, 1996]. TOMS measurements are available daily basis on a 1.25° by 1.0° grid but data may be missing because of Sun glint or contaminated with cloud [*Torres et al.*, 1998; *Cakmur et al.*, 2001]. We assume that pixels with 380 nm reflectivity higher than 0.2 are contaminated with cloud and excluded them. This criterion is chosen as the central value of the suggested range between 0.15 and 0.25 from *Cakmur et al.* [2001]. The data are then interpolated into T62 grids by averaging TOMS data within each T62 grid cell excluding the points of missing data. If data are missing at all points within a T62 grid cell, this grid cell is not given an effective value of TOMS AAI. A monthly average is calculated only at points where TOMS data are available on 10 or more days following the suggestion by *Cakmur et al.* [2001]. However, as *Cakmur et al.* [2001] suggest, detecting mineral dust by TOMS AAI is thought to contain uncertainty. On the basis of the work by *Hsu et al.* [1999], they suggest that uncertainty in daily TOMS AAI is ~0.2 and that in monthly mean is ~0.1. The uncertainty may be due to undetected subpixel clouds and the presence of biomass burning aerosols. Possible bias in monthly mean TOMS AAI due to cloud contamination of data is also examined in section 4.2.

3. Analyses of Base Case Simulation

[19] Figure 1 shows the dependence of AAI (for an amount of dust equivalent to unit AOD at 380nm) on the vertical level of dust for each of four size bins (Figure 1a) and dependence of AAI on AOD for different levels for the bin 1 (diameter range of $0.1-1.0$ μm) dust (Figure 1b). As
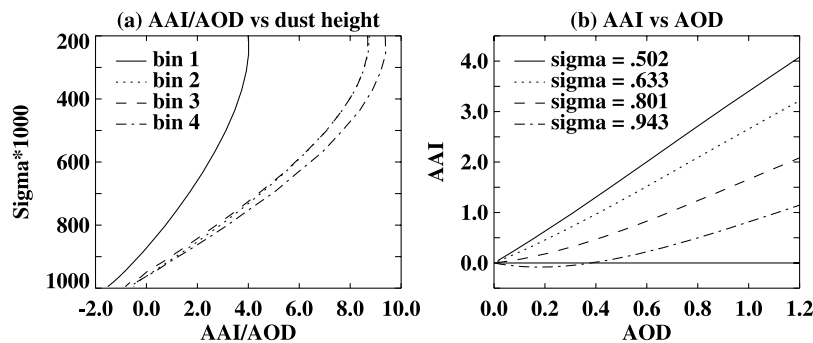
Figure 1. (a) Dependence of AAI on the vertical level (1000 times of sigma approximates pressure in hPa) of each of four size bins of unit AOD equivalent dust and (b) dependence of AAI on AOD for different levels of dust of size bin 1 (diameter range of 0.1–1.0 μm).

previously reported [*Hsu et al.*, 1999; *Torres et al.*, 1998; *Mahowald and Dufresne*, 2004], for a given AOD, AAI is higher with dust at a higher altitude and of larger particles and is nearly linear to height from the model's bottom layer to 500hPa (Figure 1a). (Both AOD and AAI are less sensitive to large particles than small particles, but AAI is more sensitive to large particles than AOD is.) For a given level of dust, AAI is nearly linear to AOD also, with different slopes for different height of dust (Figure 1b).

[20] The cross-sectional view of dust concentration and AOD and AAI values from Bodele Depression source (near 18°N, 19°E) to the west-southwest in Figure 2 demonstrate how AAI evolves as dust is carried away from its source and higher in the atmosphere (the location of the cross section is shown in Figure 3a, right)). It shows an increase of AAI from 17°E to the west following the upward transport of dust despite the almost constant AOD.

[21] Spatial distributions of MS AAI for January and July 1984 are shown in Figure 3a with corresponding AOD

distributions (Figure 3b), ratios between AAI and AOD (Figure 3c), and mass weighted mean of dust height (Figure 3d). Spatial distributions of MS AAI are similar to those of AOD. However, the AAI/AOD ratio varies between 1.0 and 3.0 over North Africa, and the spatial pattern of this ratio is similar to that of average height of dust (correlation coefficients between AAI/AOD and dust height for January and July 1984 are 0.80 and 0.86, respectively). These AAI/AOD ratios correspond to the AAI sensitivity to AOD of bin 1 dust at the middle to upper troposphere and dust in other classes in lower troposphere (Figure 1a). Figure 4 shows the spatial distribution of dust source areas as "basin factor," which is calculated from the topography and indicates the source strengths (same as "preferential source areas" of *Mahowald et al.* [2002]; Figure 4a) and actual mobilization in January and July 1984 (Figures 4b (left) and 4b (right)). Source areas along the Atlantic Coast and in Bodele Depression are active in January, and sources from southern Algeria to the west are active in July. It can
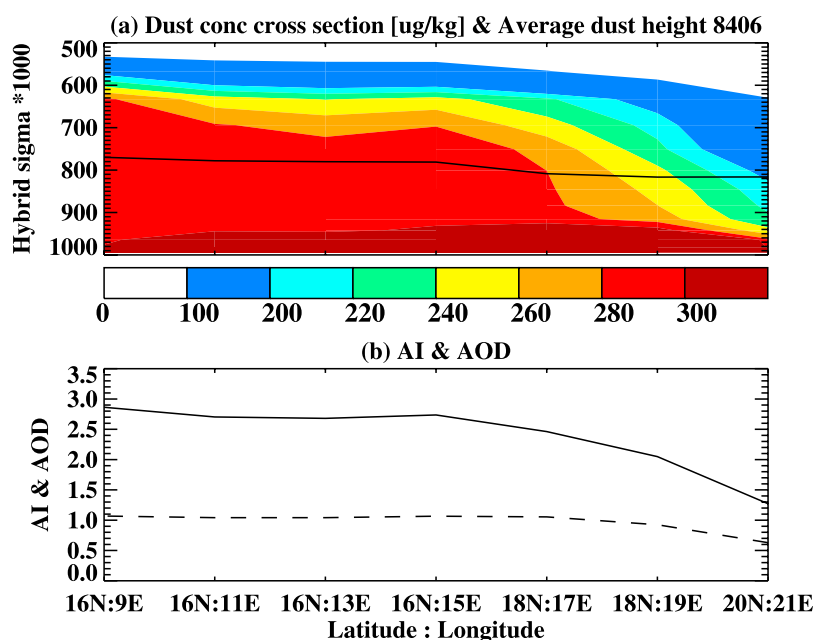

Figure 2. (a) Cross-sectional view of dust concentration (shading) and average height of dust (solid line) and (b) the AOD (dashed line) and AAI (solid line) values from Bodele Depression source (18°N, 19°E) is to the southwest (June 1984). The location of the cross section is shown in Figure 3a, right.
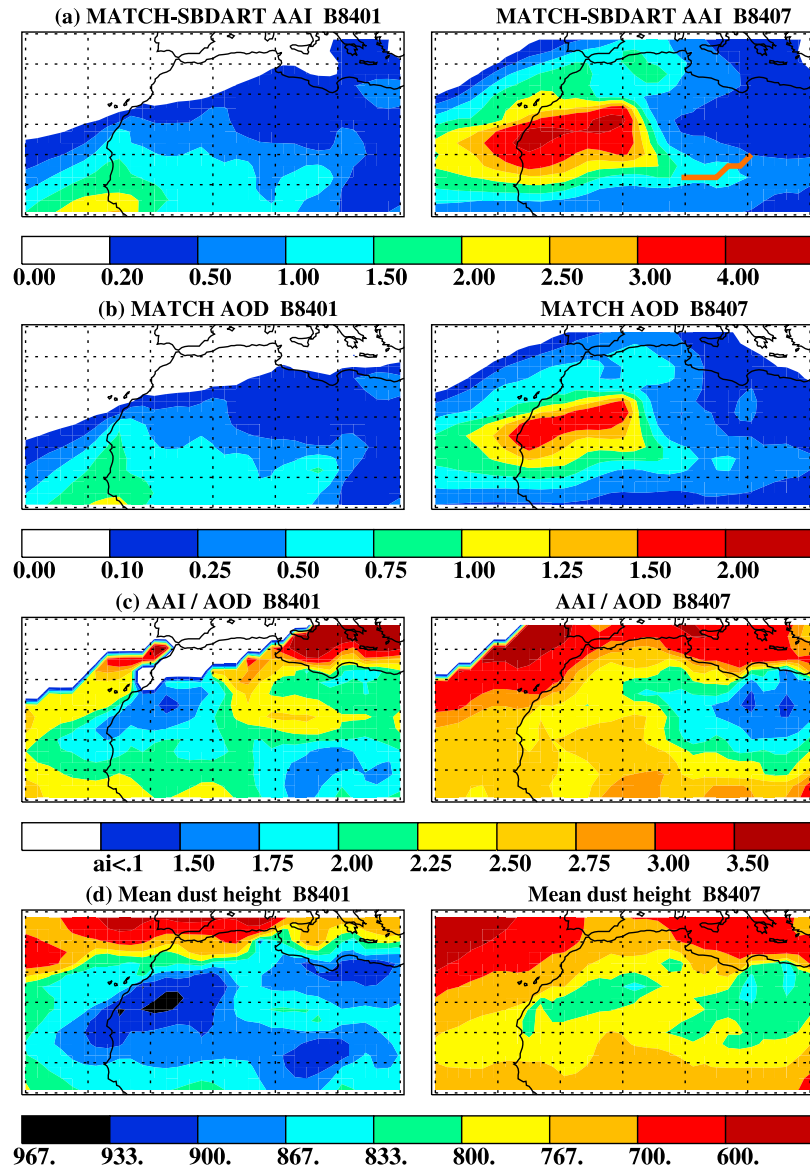
Figure 3. (a) Spatial distributions of simulated AAI, (b) AOD distributions (c), ratios between AAI and AOD, and (d) average height of dust (sigma × 1000) for (left) January and (right) July 1984. The pink thick line in Figure 3a (right) shows the location of the cross section shown in Figure 2.

be seen in Figure 3 that although both AOD and AAI become large downwind of the source regions (south in January and west in July), AAI values tend to be larger farther from the source, consistent with Figure 2.

[22] Monthly averages of satellite retrieved TOMS AAI for January and July 1984 are shown in Figure 5, in which regions where data are available on 9 days or fewer in each month are blacked out. Comparisons of Figures 3 and 5 suggest that the model is capable of capturing the rough spatial patterns of TOMS AAI, but it misses many features.

4. Evaluation of the Simplifications and Assumptions Used in the Method

[23] In the analyses presented in sections 5 and 6, MS AAI is calculated for monthly average of diurnal mean dust distributions over all days within a month using fixed satellite geometry to minimize the computation costs. However, AAI calculated in this way may lead to a bias when compared with monthly averaged TOMS AAI because of several factors. First of all, because of the nonlinear nature of AAI, AAI calculated for monthly mean dust distribution can be different from monthly average of AAIs calculated for daily dust. Second, TOMS AAI is not available for all days because of Sun glint and cloud contamination as shown in Figure 5b. Third, TOMS measurement is made once a day around local solar noon (maximum difference is about 1 hour (before or after noon) on the edges of the swath since the nodal period of Nimbus 7 satellite is 104 min (NASA, The Nimbus 7 Spacecraft System, 2003, available at http://toms.gsfc.nasa. gov/n7toms/nimbus7tech.html; British Atmospheric Data Centre (BADC), The TOMS instrument and data products, 2002, available at http://badc.nerc.ac.uk/data/toms/

(a) Dust source areas

(b) Dust mobilization [ug/m2/s] B8401 **Dust mobilization [ug/m2/s] B8407**
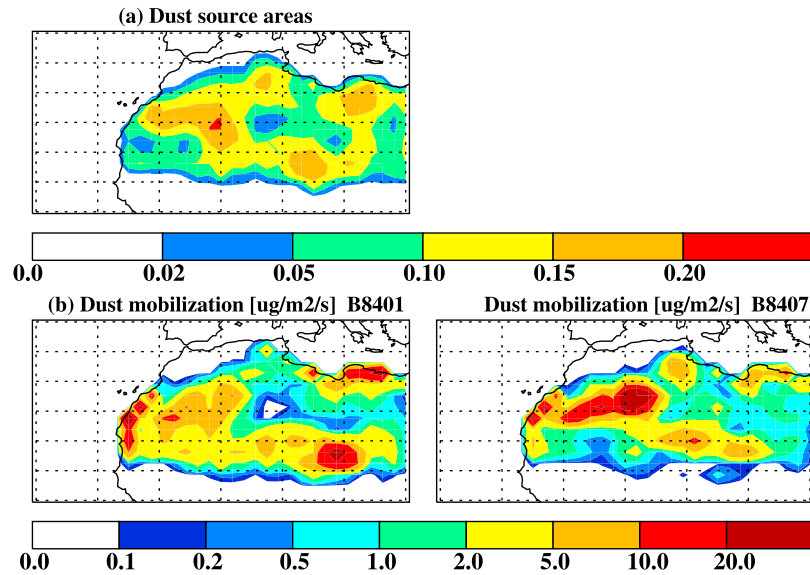
Figure 4. (a) Dust source areas (basin factor (fraction) in dry unvegetated land that indicates the source strength) and (b) actual mobilization (μg m^{-2} s^{-1}) in (left) January and (right) July 1984.

tomshelp.html). Fourth, the satellite zenith angle of Nimbus 7 TOMS varies from 0 to 51°, but it is assumed to be 0 (nadir) in the simulations. Additionally, sensitivity of MS AAI to the assumed dust particle size distribution is also demonstrated. The effects of these simplifications and assumptions in calculating monthly average AAIs are examined for January and July 1984 unless an effect is larger or of more interest in other months.

4.1. AAI for Monthly Mean Dust and Monthly Average of Daily AAI

[24] AAI calculated using monthly mean dust, atmosphere, and solar geometry are compared with monthly average of AAIs calculated for diurnal mean model results. Figure 6 shows absolute difference (former minus latter; Figure 6a) and relative difference (absolute difference divided by latter; Figure 6b) in April (Figure 6, left) and July (Figure 6, right). Differences are small in January (only up to 0.05). The calculation with monthly mean dust and other conditions overestimates AAI by up to 0.32 and 18% in April and 0.44 and 11% in July where AAIs are high, and underestimates it by up to 0.1 and 30% in April occur where AAIs are relatively small (there is almost no underestimate in July). The relative errors are largest in April in both the maximum magnitude and frequency (i.e., number of grid points). If we look at grid cells where AAI is larger than 0.5
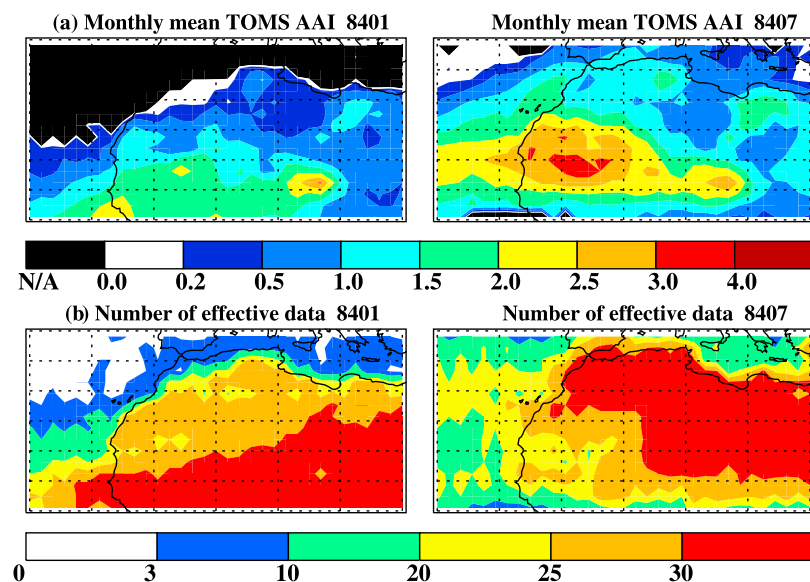
(a) Monthly mean TOMS AAI 8401 **Monthly mean TOMS AAI 8407**

(b) Number of effective data 8401 **Number of effective data 8407**

Figure 5. (a) Monthly averages of TOMS AAI and (b) number of days for which TOMS measurements with under-threshold cloud contamination are available for (left) January and (right) July 1984.
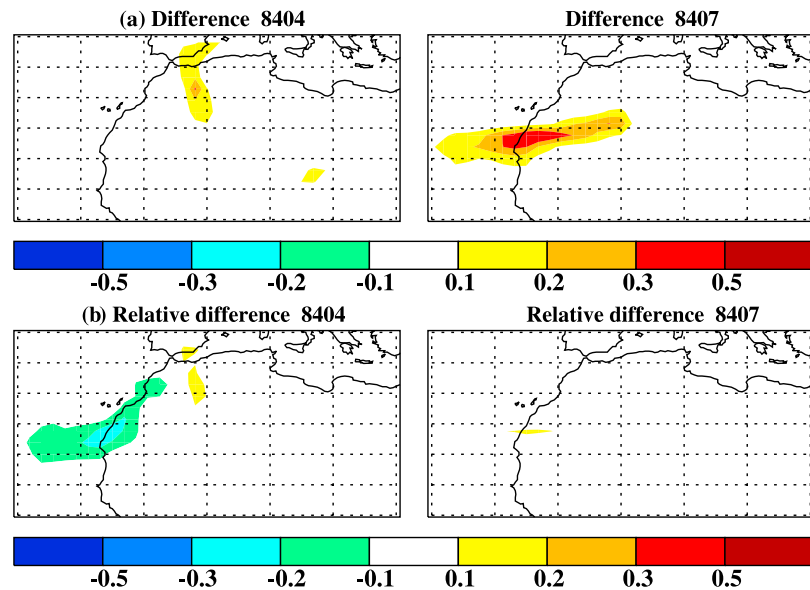
Figure 6. (a) Absolute (the former minus the latter) and (b) relative (absolute divided by the latter) differences between MS AAI calculated for monthly mean dust and atmosphere and monthly average of MS AAIs for daily dust and atmosphere in (left) January and (right) July 1984.

(70.1% of all) to avoid small denominators, the maximum relative errors are +18% and −12%, and number of grid cells with relative errors exceeding ±10% are ~3% in April.

4.2. Monthly Averages for All Days and for Days When TOMS Data Are Available

[25] Figure 7 shows the absolute (Figure 7a) and relative (Figure 7b) differences between MS AAI calculated for simple monthly average dust (using data of all days in a month) and reconstructed (from data of days when TOMS data are available) monthly average of dust and atmosphere

in January (Figure 7, left) and July (Figure 7, right) 1984. In July, the simple average is larger than reconstructed average by more than 0.3 (more than 10%) over large areas from the peak AAI region (western Sahara; southwest or downwind of the source region in Figure 4) to the west with the maximum difference of 0.99 (64%) off the west coast of North Africa. In January also, the simple average is larger by more than 30% over north to central Sahara although the difference in actual values are much smaller than in July. However, over the Mediterranean in July, the simple monthly average MS AAI is smaller by over 0.3 and
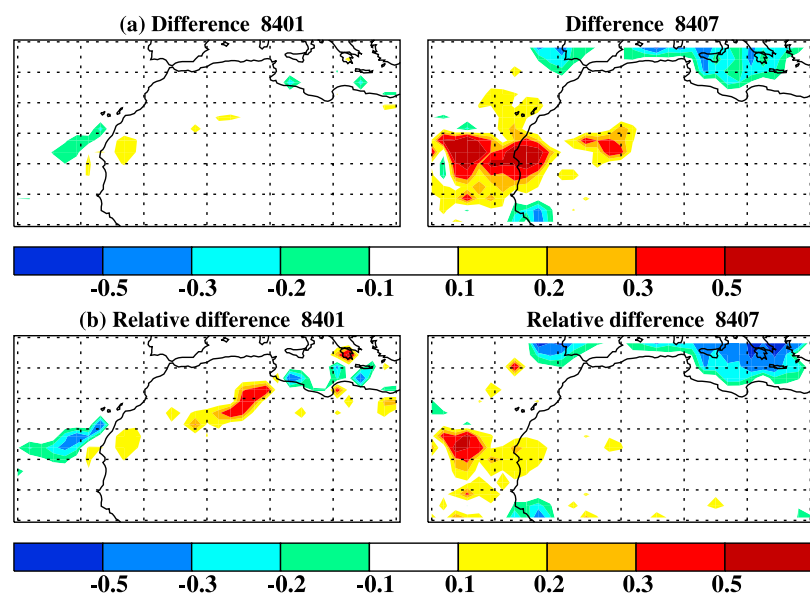
Figure 7. (a) Absolute and (b) relative differences between simple and reconstructed (average over days when TOMS data are available at a given grid point) monthly averages of MS AAI for (left) January and (right) July 1984.

30%. Relative error exceeds 30% (positive or negative) in 3% in January and 8% in July of the grid cells with reconstructed average AAI of over 0.5.

[26] These errors may be a result of cloud screening using the reflectivity criterion and correlation between dust loading and cloud amount. The reflectivity at 380 nm becomes higher with higher column loading of dust. If reflectivity criterion higher than 0.15 is chosen, this value is not reached with maximum dust loading in the clear-sky condition (similar to *Cakmur et al.* [2001]). However, reflectivity of grid cells with high dust loading can exceed the criterion with less subgrid clouds, and hence they can be excluded from the average preferentially. This can lead to a lower AAI in the reconstructed monthly averages excluding pixels and days of high reflectivities. Another possibility is that there tends to be less dust when TOMS data are available (which is when there is less cloud). This may suggest a positive correlation between dust and cloud amounts over this region, as seen in the case of low thin clouds by *Mahowald and Kiehl* [2003].

4.3. AAIs Calculated for Local Noon Dust and Diurnal Mean Dust

[27] Since diurnal variabilities of dust mobilization and vertical mixing are large [*Luo et al.*, 2004], there expected to be difference between AAI at local noon and AAI calculated for diurnal mean dust. Figure 8 shows absolute (Figure 8a) and relative (Figure 8b) differences between AAIs calculated for monthly average of dust and atmosphere at local solar noon (1200 UT in 5°W−5°E, 1120 UT in 5−15°E and 1040 UT in 15−25°E) and monthly average of diurnal mean dust and atmosphere in January (Figure 8, left) and July (Figure 8, right). AAI calculated for monthly average of diurnal mean data is smaller than that of local noon data by more than 0.3 and 20% over Bodele Depression and northeastern Libya (maximum is 0.40 and 31%) in January and by more than 0.5 and 10% (maximum 0.63 and 22%) in the high AAI region over southwestern Algeria and northern Mali in July. This suggests that diurnal means underestimate AAI in source regions (see Figure 4) and sometimes overestimate it in nearby downwind regions (e.g., south of Bodele Depression in January).

4.4. Difference Due to Satellite Viewing Angles

[28] AAIs are calculated with satellite zenith angles 0°, 15°, 30°, and 45° and corresponding solar zenith and azimuth angles for satellite and solar positions and latitudes. Figure 9 shows absolute (Figure 9a) and relative (Figure 9b) errors associated with calculating AAI using a nadir satellite viewing angle while the actual satellite zenith angle is 45° in April (Figure 9, left) and July (Figure 9, right). The calculated viewing angle at a given point in the domain is approximated by 45° (i.e., falls between 37.5° and 51°, the latter of which is the maximum viewing angle of the TOMS satellite sensor (NASA, 2003, http://toms.gsfc.nasa.gov/n7toms/nimbus7tech.html; BADC, 2002, http://badc.nerc.ac.uk/data/toms/tomshelp.html)) from ∼30% (at 40°N) to 45% (at 10°N) of the time depending on the latitude (average for all latitudes is 39%).

[29] This analysis shows that for satellite viewing zenith angles larger than zero, the error due to using viewing angle of 0° is always negative and has small seasonal and spatial

structures. With satellite zenith angle of 45°, relative error exceed 20% in ∼3% of points where AAI is larger than 0.5, with maximum of 24%. With satellite viewing angle of 30°, errors are much smaller and points where relative error exceeds 10% are ∼5% of all points with AAI larger than 0.5, and the maximum relative error is 13%. The average maximum relative error (weighted with the relative frequencies with which the satellite viewing angle falls into the ranges of the four given angles) is ∼12% in both April and July. Since the differences are one-sided (always negative) and have small seasonal and spatial structures (Figure 9b), and since the model has been tuned to give a desired magnitude of AAI, some of these differences must have already been compensated. Therefore their effects on comparisons between monthly averaged observed and simulated AAIs are not thought to be large.

4.5. Difference Due to Assumed Particle Size Distribution

[30] In this study, mass fractions of four size bins (0.1−1.0, 1.0−2.5, 2.5−5.0, and 5.0−10.0 μm in "diameter") in the source are assumed to be 0.1, 0.3, 0.3, and 0.3, respectively. These fractions represent much more dust in the smaller size fractions than other studies [e.g., *Ginoux et al.*, 2001]. Additionally, recent field observations suggest that previous modeling studies may underestimate particle sizes of transported African dust [*Colarco et al.*, 2003; *Grini and Zender*, 2004]. For this sensitivity study, AAI is calculated using the source mass fractions of 0.03, 0.17, 0.41, and 0.39 for the same four size bins. These fractions are calculated from the mobilization scheme incorporating saltation-sandblasting dust production mechanism described by *Grini and Zender* [2004] (this is the global result and different from their results for Sahara shown in their paper (C. S. Zender, personal communication, 2005)). Thus the new estimates of appropriate size distributions give much less dust in the smaller two size bins (1/3 to 1/2) and more in the larger size bins compared with the size distribution used in the base case.

[31] The values of AAI and AOD become nearly half of the original values and as a result, the ratios of AAI/AOD do not change very much (not shown). This is mainly due to smaller radiative effects per unit mass (mass extinction coefficient) of larger particles. Over North Africa, the modified mass fraction case has slightly larger AAI/AOD, due to the larger fraction of large particles close to the source regions (Figure 1). Next we look at the impact of changing the size distributions on the spatial distribution of MS AAI (shown in Figure 10). These results show that there are only small relative differences in the spatial distribution. Thus changing the size distribution between different bins changes the mean AAI, but not the spatial or temporal distribution of the AAI.

4.6. Combined Effect

[32] Errors associated with the simplifications examined in sections 4.1, 4.2, and 4.3 are spatially heterogeneous and so they may impact our comparisons between model simulated and observed AAI distributions. Additionally, they may add nonlinearly when included together, so here we look at the combined impact of several of these sensitivities. Figure 11 shows the errors when the effects in sections 4.1,
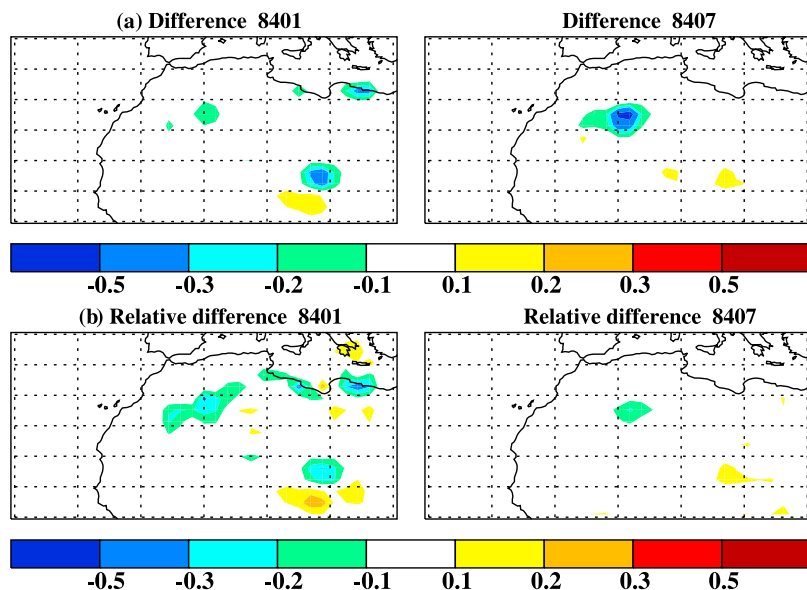
(a) Difference 8401   **Difference 8407**

(b) Relative difference 8401   **Relative difference 8407**

Figure 8. (a) Absolute and (b) relative differences between monthly averages of MS AAI calculated for daily mean dust and atmosphere and MS AAI for dust and atmosphere at local solar noon in (left) January and (right) July 1984.

4.2, and 4.3 are examined at the same time, that is, average of AAI values calculated for dust and atmosphere at local noon of days of the month on which TOMS data are available. Effects of satellite geometry and particle size distribution are not combined here because they are spatially much less heterogeneous, combining them is technically more complicated, and the significance of combining them is not as clear. Note that Figure 11 does not have values west of 5°W and east of 25°E due to the lack of local noon model outputs in these regions. They look similar to super-positions of the separate cases (compare Figures 11a (right)

and 11b (right) with those in Figures 6, 7, and 8), and no strong nonlinearity is apparent. The absolute error is up to −0.41 and 0.24 in January and −0.57 and 0.64 in July, and the relative error is up to about −60% and 20% in both January and July where AAI in combined sensitivity case is over 0.5. Relative error exceeds 30% (positive or negative) in 4% in January and 9% in July of all grid cells with AAI over 0.5. These are comparable to the case of reconstructed monthly average (section 4.2 and Figure 7). Combined errors outside the region of Figure 11 are examined by simply superposing the errors shown in Figures 6 and 8 (not
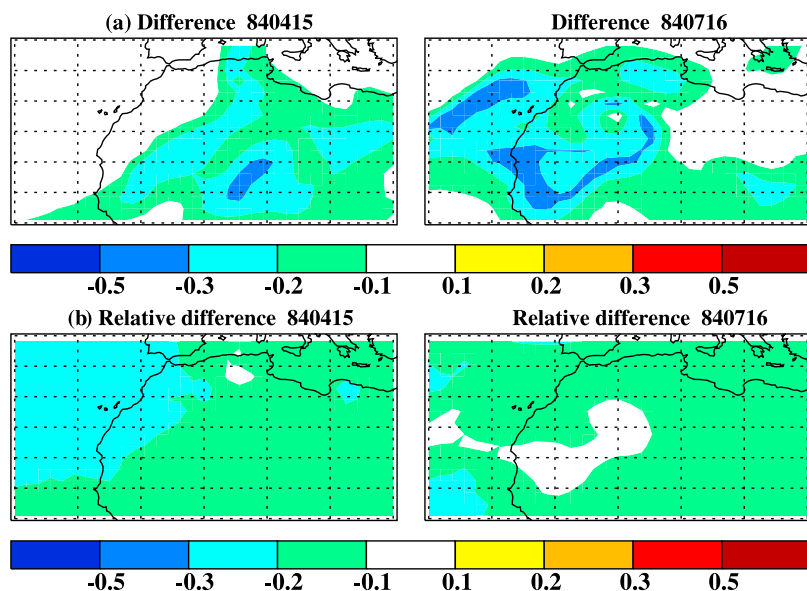
(a) Difference 840415   **Difference 840716**

(b) Relative difference 840415   **Relative difference 840716**

Figure 9. (a) Absolute and (b) relative differences between MS AAI calculated using nadir looking viewing angle and using 45° viewing zenith angle in (left) April and (right) July 1984.
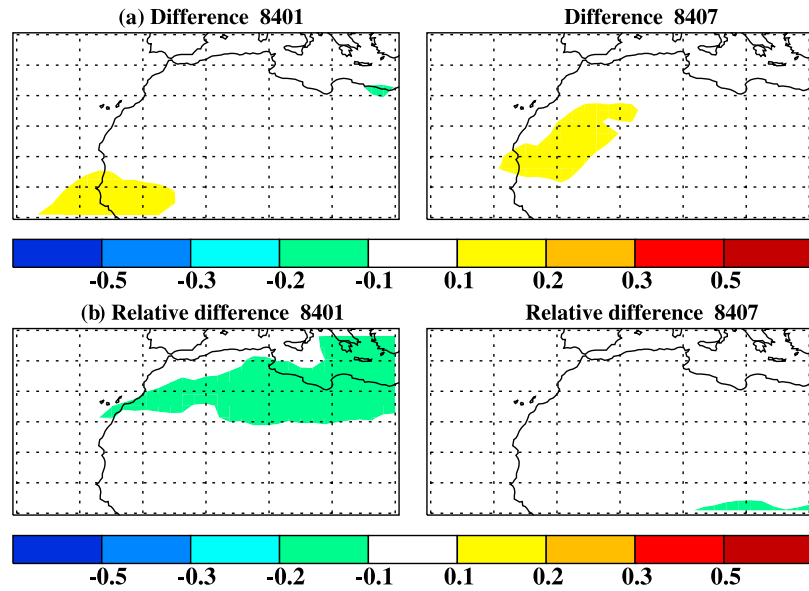
Figure 10. (a) Absolute and (b) relative differences between MS AAI calculated using original particle size distribution (mass fraction of 0.1, 0.3, 0.3, and 0.3 in four size bins) and modified one (0.0325, 0.174, 0.409, and 0.385 in the same bins) for (left) January and (right) July 1984.

shown). It creates a region over western Sahara (west of 10°W) to the Atlantic in July where errors add up to a maximum of a little over 1 (over 80%) over the ocean.

[33] The errors associated with simplifications in timing of measurements and averaging are thought to introduce an important level of uncertainty to our comparisons between simulations and observations. Errors due to simplification in satellite geometry and assumption of particle size distribution add the uncertainty to lesser degree. These uncertainties are large, but not larger than the errors and uncertainties

seen in the later sections due to model and observational differences.

5. Analyses of Different Source Processes

[34] As described in section 2, simulations are conducted for four types of dust sources: 100% topographic depression source (B), 50% of topographic depression source combined with 50% of new desert source (BD) and with 50% of cultivated land source (BC), and 85% of topographic
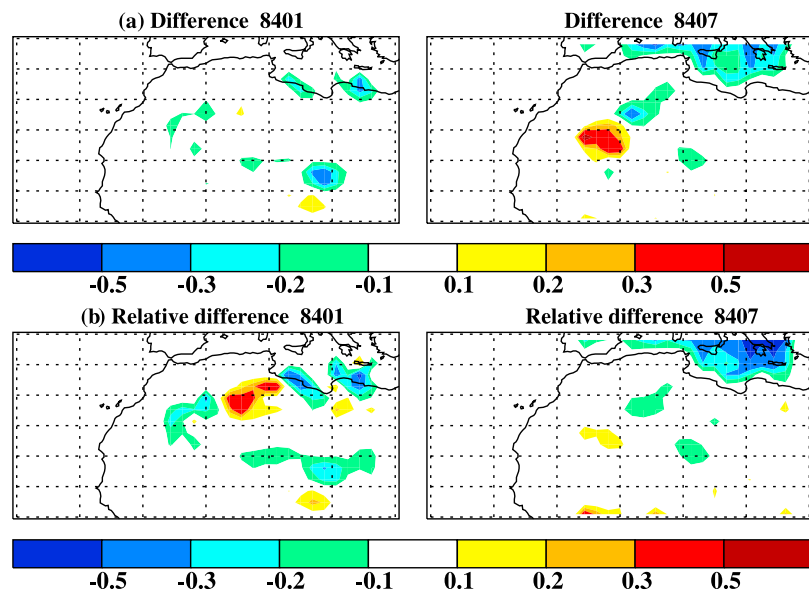

Figure 11. Combination of the effects examined in Figures 6, 7, and 8. (a) Absolute and (b) relative differences between MS AAI calculated using simple monthly average of daily mean dust and atmosphere and average of MS AAI calculated for dust and atmosphere at local noon on days of the month for which TOMS data are available in (left) April and (right) July 1984.
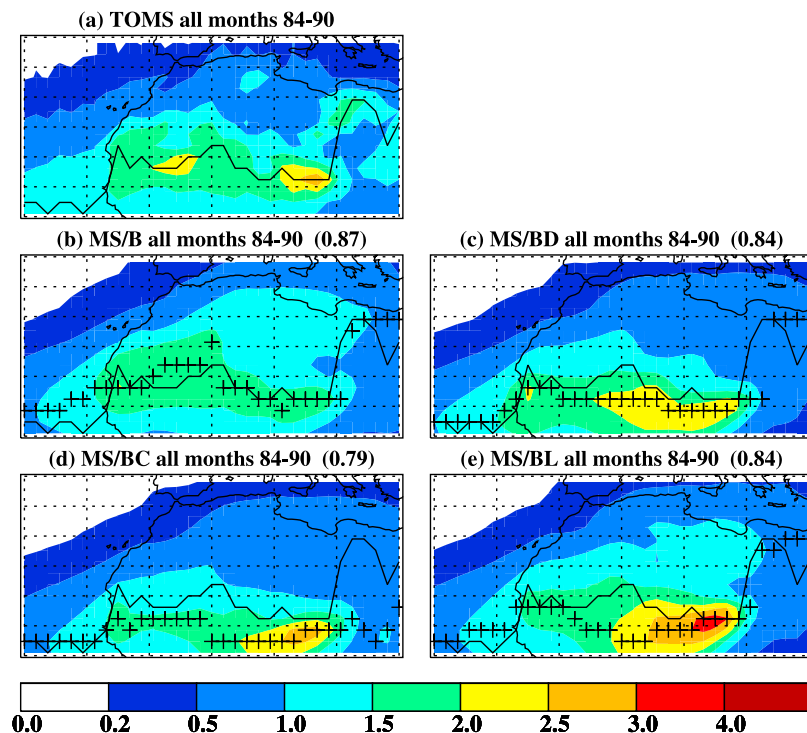
Figure 12. Distributions of AAIs averaged over all months and years from (a) TOMS observation and (b) MS/B (MATCH-SBDART case B), (c) MS/BD, (d) MS/BC, and (e) MS/BL simulations. The solid line and pluses show the latitudes at which TOMS and MS AAI, respectively, maximize on each longitude. Numbers in parentheses are correlation coefficients between MS and TOMS AAIs.

depression source with 15% source from Lake Chad and Bodele Depression region (BL). AAIs and other quantities are averaged over the whole domain (10.5–39.0°N; 30.0°W–30.0°E) as well as Sahara (23.8–35.2°N; 15.0°W–30.0°E), Sahel (10.5–21.9°N; 20.6°W–30.0°E), and Bodele (12.4–20.0°N; 13.1–20.6°E; within Sahel) subdomains and are analyzed. We compare simulated AAI with different types of sources against TOMS AAI in order to assess which source type is most consistent with observations. Any bias in simulated AAI can be due to the biases in either the column loading or the vertical profile of dust, both of which are a result of mobilization, transport and deposition processes. Atmospheric processes that may lead to a bias in AAI are examined in section 6 through sensitivity studies using a different input meteorology and source scheme.

5.1. Spatial Distributions

[35] Figure 12 shows the distributions of AAIs from TOMS observation (Figure 12a) and MS/B (case B (Figure 12b)), MS/BD (Figure 12c), MS/BC (Figure 12d), and MS/BL (Figure 12e) simulations averaged over all months from 1984 to 1990. The TOMS AAI plots such as Figures 12a, 5a, and 5b show local maxima of AAI over several regions, which is consistent with dust source regions identified by *Prospero et al.* [2002]. The correlation coefficients of spatial distributions of simulated AAIs with observation are between 0.79 (case BC) and 0.87 (case B) (correlation coefficient in each case is given in the parentheses in Figure 12). Determining if these values are statistically distinct from each other is made complicated

by the fact that dust loadings are spatially correlated because of horizontal transport. The correlations of nearby grid cells reduce the degree of freedom and hence lower the probability that two correlation coefficients are statistically distinguishable, however the factor by which it is reduced is not obvious. In Table 1 we show the factors by which we can reduce the degrees of freedom and still obtain statistically significantly different correlations (i.e., they are distinct exactly at 95% confidence level). We assume that this factor must be great than five in our analysis, due to spatial correlations. Even though the spatial correlation coefficient of MS/B AAI with observation is a little higher than those of other cases, the differences are statistically insignificant and MS/B AAI is worse in terms of capturing the observed strength of AAI over Bodele Depression and western Sahel and generally overestimates AAI over Sahara especially over southwestern Algeria and western Sahara in July (Figure 5). As a result, case B simulation underestimates the ratios of AAI values of Sahel and Bodele to Sahara (Figure 13). The other three simulations overcorrect these ratios (i.e., D, C, and L sources are too strong), and therefore a linear combination of the different sources can be selected to best match the observations. The observed Sahel/Sahara ratio is obtained when D or C sources are ~25% of the total dust source (not shown).

[36] As shown in Table 1, the spatial distribution of AAI over Sahel is better reproduced in case B (correlation coefficient with observation is 0.81) than other cases in which the Sahel dust plume seems to be shifted to the south (correlation coefficients in cases BD, BC and BL are 0.64, 0.42, and 0.69, respectively). The spatial correlation in case

Table 1. Correlation Coefficients of Simulated Spatial Distributions, Seasonal Changes, Time Series, and Anomalies of AAI With Observed Ones Over the Whole Domain and Subdomains[a]

Case Domain	B	Threshold Correlation[b]	BD	BD 35%	BD 25%	BD 15%	BC	BC 35%	BC 25%	BC 15%	BL
Spatial											
Whole	0.87		0.84	0.87	0.88	*0.89*	0.79	0.85	0.88	*0.89*	0.84
Sahel	*0.81*		0.64	0.71	0.75	0.79	**0.42**	**0.58**	0.69	0.77	0.69
Threshold factor[c]			3.6	1.7	0.67	0.12	**10.**	**5.2**	2.0	0.28	2.0
Seasonal											
Whole	*0.92*	0.59	**0.57**	0.71	0.79	0.85	0.59	0.73	0.81	0.86	0.69
Sahara	*0.86*	0.37	0.66	0.75	0.79	0.83	0.74	0.80	0.82	0.84	0.72
Sahel	*0.89*	0.46	**0.45**	0.59	0.68	0.77	**0.43**	0.58	0.68	0.78	0.55
Bodele	*0.77*	0.10	0.40	0.50	0.58	0.66	0.31	0.42	0.51	0.62	0.51
Time Series											
Whole	*0.79*	0.64	**0.50**	**0.61**	0.67	0.73	**0.52**	**0.63**	0.69	0.74	**0.53**
Sahara	*0.74*	0.56	**0.55**	0.63	0.67	0.70	0.62	0.67	0.70	0.72	0.58
Sahel	*0.76*	0.60	**0.41**	**0.51**	**0.59**	0.66	**0.39**	**0.51**	**0.59**	0.67	**0.43**
Bodele	*0.64*	0.43	**0.35**	0.44	0.50	0.56	**0.28**	**0.37**	0.45	0.53	**0.41**
Anomaly											
Whole	0.17		0.29				0.27				0.14
Sahara	0.09		0.20				0.18				0.07
Sahel	0.24		0.27				0.26				0.15
Bodele	0.26		0.17				0.16				0.13

[a]Correlation coefficients of simulated spatial distributions are the correlated individual grid cells averaged over all years and months, seasonal changes are the correlated 12 months averaged over all years, time series are correlated for all months in the 7-year period individually, and anomalies are correlated for all months in the period but seasonality is removed. Numbers with percent indicate the fraction of second source (e.g., case BD35% is a mixture of 65% topographic and 35% new desert sources), and it is 50% for BD and BC and 15% for B. The italic correlation coefficients are highest ones in the different mixtures of the same combinations of sources. Bold indicates that the correlation coefficients are statistically distinct from those in case B with a 95% confidence level. For spatial correlations, this judgment is made using reduced degree of freedom by factor of 5.

[b]Threshold correlation coefficient; a correlation smaller than this value is significantly smaller than the correlation in case B with a 95% level.

[c]Threshold factor of reduction of degree of freedom; the differences of the shown spatial correlations for Sahel from that in case B (0.81) become insignificant with a 95% level if degree of freedom is reduced by more than this factor.

BC is statistically significantly lower than in case B with the reduced degree of freedom by factor of over 10. Dust mobilizations with D (new desert only) and C (cultivation only) sources (not shown) have local maxima about 1 to 2 grid boxes (1.8° to 3.6°) south of that with B source in the Bodele subdomain. Also the southward bias is prominent from November to May (not shown), which coincide the seasons in which the combination sources (i.e., BD, BC, and BL) overestimate AAI (discussed in section 5.2) and northeasterly winds dominate in the lower troposphere over Sahel. Therefore the southward biases seen in the annual average simulated AAI distributions with combination sources are considered as a product of the difference in locations of dust source and the bias in seasonality of dust mobilization.

5.2. Seasonality of AAI by Region

[37] Figure 14 shows the seasonal change of observed and simulated AAIs averaged over all years (1984–90) over the whole domain (Figure 14a), Sahara (Figure 14b), Sahel (Figure 14c), and Bodele (Figure 14d) subdomains. Over the whole domain, MS/B simulation overestimates AAIs in March to May and underestimates in July to September. This seems to be due to overestimates of AAIs over Sahara in boreal winter to spring and underestimates in Sahel and especially in Bodele in summer to early fall. The magnitudes of summertime underestimates in Sahel and Bodele are large and the balance between these and the springtime overestimate in Sahara is considered as the reason for the bias in the Sahel/Sahara and Bodele/Sahara ratios in Figure 13. While these annual average ratios are improved

by adding other sources (i.e., cases BD, BC, and BL), the large deficiencies in summer along with the overestimates in spring in Sahel and Bodele are made worse by addition of sources as shown in Figure 14 and Table 1. Especially over Sahel, the correlations of simulated monthly AAIs (averaged over all years) with observed ones are statistically significantly higher in case B than in cases BD and BC. The seasonality of AAI is further analyzed using different wind and dust schemes in section 6 in order to better understand the uncertainties associated with these analyses.

5.3. Interannual Changes by Region

[38] Figure 15 shows the interannual changes of observed and simulated AAIs averaged over all months. All simulations show basically the similar patterns in terms of year-by-year changes as well as increasing trends in the period, and these patterns do not agree with those of observations. Correlation coefficients between observations and simulations are negative in all cases and regions (not shown), and combination sources do not improve the correlations.

[39] Correlation coefficients of simulated AAIs of all months in the 7-year period (seasonality is included) with observed ones are significantly higher in case B than in other cases over all regions except Sahara (Table 1). However, all simulations fail to reproduce observed anomalies of AAI (changes of monthly AAI with average seasonality removed) (Table 1).

5.4. Optimum Source Mixture and Acceptable Range

[40] As shown above, the case BD and BC simulations correlate with the observations statistically significantly
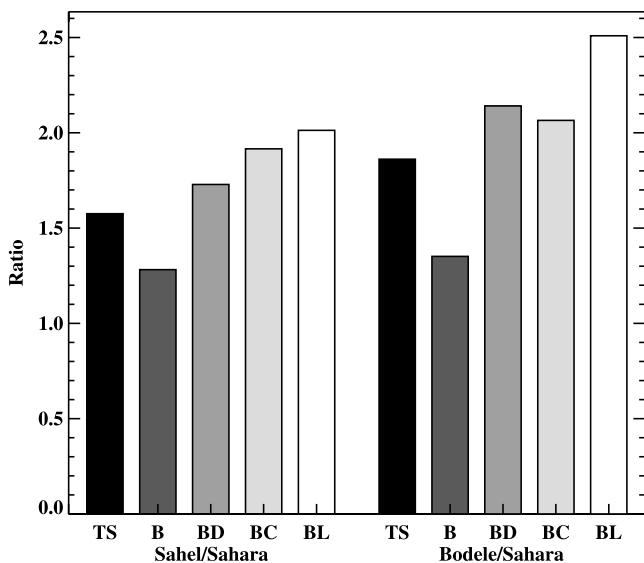
Figure 13. Ratios of annual average AAI values of Sahel (10.5–21.9°N; 20.6°W–30.0°E) and Bodele (12.4–20.0°N; 13.1–20.6°E) to Sahara (23.8–35.2°N; 15.0°W–30.0°E). "TS" indicates "TOMS," and others are "MS" with indicated source types.

worse than the case B simulations in spatial (BC only) and temporal (seasonal and over all 84 months) comparisons. As mentioned in section 5.1, simulations using lower fractions of new desert and cultivation sources suggest that the optimum mix of sources in terms of Sahel/Sahara ratio is 25% of new desert (D) or cultivation (C) (and 75% of topographic (B)) sources. However, as summarized in Table 1, it is 15% of D or C source in terms of spatial correlation over the whole domain and 0% over Sahel. Temporal (seasonal and time series) correlations are highest with 100% B source over all regions. D and C sources need to be less than 25% in order for the all correlations to be statistically indistinct from case B.

[41] Even though the domain has been chosen to minimize the influences of biomass burning smoke, its effects in the seasonal comparisons cannot be ruled out. If December, January, and February, when biomass burning is active near the southern boundary of the domain [e.g., *Menaout et al.*,

1991; *Stroppiana et al.*, 2000], are excluded, the time series correlations of mixed source cases with observations become higher by up to 0.13 over Sahel and Bodele subdomains, while those correlations do not change almost at all with case B. In this case, the optimum mix is still 100% topographic source, but the new desert and cultivation sources can be up to ∼35% to keep the time series correlations indistinct from case B. However, we cannot judge whether these changes happened due to biomass burning or just by chance.

6. Sensitivities Studies Using Different Wind Data Sets and Dust Mobilization Schemes

[42] Analyses in the previous sections are based on simulations using NCEP reanalysis and the DEAD mobilization scheme. In this section, sensitivity studies are performed using different combinations of meteorological data sets and dust mobilization schemes. The primary purpose of these sensitivity studies is to examine how robust the results in the previous section are to changes in the model configuration. If the results from the sensitivity studies are quite different from the original study (and this is actually the case), the simulations are analyzed in detail in attempt to identify the factors that cause the observed differences.

[43] The sensitivity studies use the topographic depression source (case B), either NCEP or DAO meteorological data set, and either DEAD or GOCART dust mobilization scheme. A simulation using DAO wind and GOCART scheme for mobilization but NCEP for transport is also performed. Hereafter, these configurations are expressed as B-NDN, B-DDD, B-DGD, and B-DGN, with letting the first letter (B) indicate the topographic source, the first and last letters after the hyphen the meteorological data set (i.e., NCEP or DAO) used for mobilization and transport, respectively, and the second the mobilization scheme (i.e., DEAD or GOCART). Additionally, the DGD simulation is performed with 50% topographic depression and 50% cultivation sources (case BC-DGD). All simulations are conducted for February to November 1995 except B-NDN which is simulated for all months in 1995. These simulations correspond to those summarized by *Luo et al.* [2003, Table 1]. Since TOMS AAI is unavailable in this year for comparisons unfortunately, average TOMS AAIs over 1984–1990 are used for comparisons. Comparing
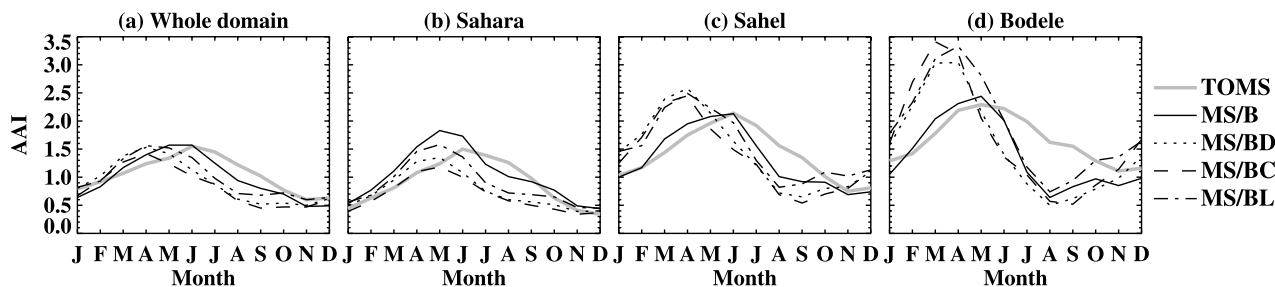

Figure 14. Seasonal changes of TOMS and MS AAIs averaged over all years (1984–1990) over (a) the whole domain (10.5–39.0°N; 30.0°W–30.0°E) and (b) Sahara (23.8–35.2°N; 15.0°W–30.0°E), (c) Sahel (10.5–21.9°N; 20.6°W–30.0°E), and (d) Bodele (12.4–20.0°N; 13.1–20.6°E) subdomains.
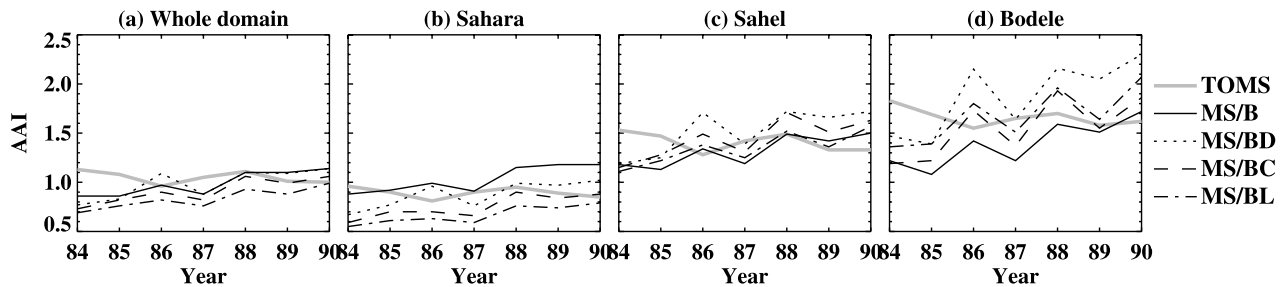
Figure 15. Interannual changes (averaged over all months) of TOMS and MS AAIs averaged over (a) the whole domain and (b) Sahara, (c) Sahel, and (d) Bodele subdomains.

AAI simulated for 1995 with climatological TOMS AAI should also be noted as a source of uncertainty.

6.1. Spatial Distributions

[44] Figure 16 shows the AAI distributions predicted by these simulations averaged over February to November 1995. TOMS AAI averaged over February to November and 1984 to 1990 minus and plus standard deviation of interannual variability at each point are also shown in Figures 16a and 16b, respectively, and these give the likely range of TOMS AAI in 1995 if there is no trend in decadal timescale. Figure 16c is the result of the same model configuration as Figure 12b. All the simulations for 1995 (Figures 16c–16g) predict AAI larger than the higher limit of the range based on mean and variability between 1984 and 1990 (Figure 16b) but by much higher degrees in cases using DAO wind for mobilization (Figures 16d–16g) than in case using NCEP wind (Figure 16c). The simulations using DAO for mobilization also seem to produce spatially less heterogeneous patterns of AAI than that using NCEP. This may be due to less spatial variability in wind speed in original DAO data and/or the interpolation of data from $2.5° \times 2.5°$ grids [*Luo et al.*, 2003]. The simulation using 50% cultivation source (Figure 16g) produces AAI distribution highly concentrated over eastern Sahel.

[45] The spatial distributions of AAI with DAO mobilization (cases B-DDD, B-DGD, and B-DGN) correlate with observation (averaged over February to November 1984 to 1990) better (correlation coefficients are 0.86, 0.85, 0.84, respectively) than with NCEP (0.78) but not in statistically significant manner. The correlation in case BC-DGD is lower (0.72) than in the case B-DGD, as we saw in section 5 that BC-NDN less correlates with observations than B-NDN does in 1984–1990. The spatial correlation of DGD simulation with the observation becomes highest (0.87) when the mixture of C source is 15% and the correlation becomes statistically significantly lower (0.79) than this with 40% C source (when the degree of freedom is reduced by factor of 5; see section 5.1). Sahel/Sahara and Bodele/Sahara ratios are somewhat improved with DAO mobilization but they are still lower than the observed values while they are overestimated with BC source (Sahel/Sahara ratios for TOMS, B-NDN, B-DDD, B-DGD, B-DGN, and BC-DGD are 1.54, 1.02, 1.24, 1.27, 1.21, and 2.2, respectively, and this ratio with DGD simulation matches the observation when C source is ~20%). However, the observed AAI distribution within the Sahel subdomain is best reproduced in B-NDN simulation (correlation coefficients with B-NDN,

B-DDD, B-DGD, B-DGN, and BC-DGD are 0.81, 0.77, 0.75, 0.76, and 0.18, respectively) and the correlation with BC-DGD is statistically significantly lower than other cases. The correlation of DGD simulation is highest (0.75) with 0% C source (case B-DGD) and, assuming the distribution of dust sources is the dominant cause of the bias in the simulations, cultivation source needs to be less than 40% to keep the spatial correlation within Sahel not significantly worse than this case, and at this mixture the correlation coefficient within Sahel is 0.51.

6.2. Seasonality of AAI by Region

[46] Figure 17a shows the seasonalities of AAI simulated with different meteorological data sets and mobilization schemes averaged over the whole domain and the three subdomains (i.e., Sahara, Sahel, and Bodele). Also shown are the seasonalities of TOMS AAI (with error bars for plus and minus interannual standard deviations) and B-NDN simulation for 1984–1990, but in order to focus on the comparisons of seasonalities, both of their values (as well as the standard deviations) are increased by 26% so that the annual average AAI in B-NDN over the whole domain for 1984–1990 equals that for 1995. Notice that changing the meteorology does not change the seasonality much (B-DDD versus B-NDN), while changing the source scheme does change the seasonality (B-DGD versus B-DDD).

[47] In the whole domain and all subdomains, simulations using GOCART (B-DGD, B-DGN, and BC-DGD) do not produce the large deficiency in summer that NDN simulations with all source types (i.e., all simulations in section 5) produce, even though B-DDD does produce it using the same wind as B-DGD. Therefore the source parameterization may be responsible for the deficiencies in summer time AAI seen in section 5. On the other hand, simulations using the GOCART source scheme with either set of winds tends to overestimate AAI in fall and underestimate it in spring, which is opposite to simulations using the DEAD scheme with either DAO or NCEP winds—cases B-DDD or B-NDN. These effects are thought to be combined with the effects of combination sources to produce the seasonal pattern seen in case BC-DGD, where the summer time deficiency has disappeared and overestimates in fall to early spring have become prominent in Sahel and Bodele. Although the seasonal changes are not statistically analyzed because of a small size of samples (i.e., number of months; 10) here, the seasonal pattern of BC-DGD simulation is obviously the least consistent with the observed seasonal pattern, as in the cases of combination sources in the
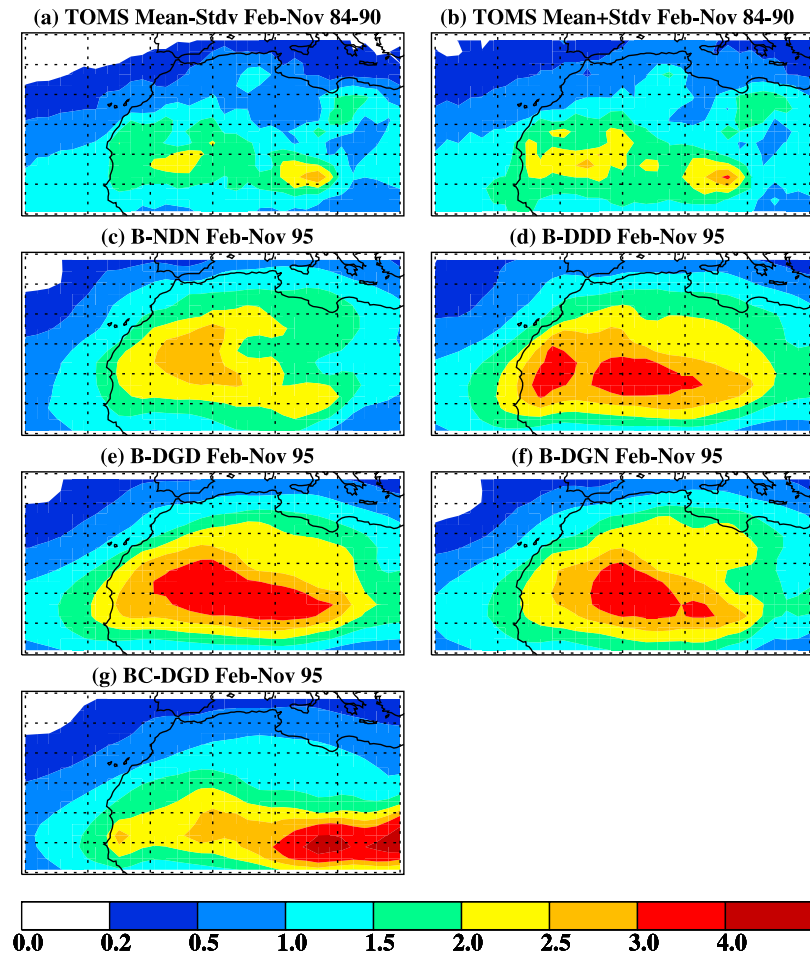
(a) TOMS Mean-Stdv Feb-Nov 84-90   **(b) TOMS Mean+Stdv Feb-Nov 84-90**

(c) B-NDN Feb-Nov 95   **(d) B-DDD Feb-Nov 95**

(e) B-DGD Feb-Nov 95   **(f) B-DGN Feb-Nov 95**

(g) BC-DGD Feb-Nov 95

0.0   0.2   0.5   1.0   1.5   2.0   2.5   3.0   4.0

Figure 16. TOMS AAI averaged over 1984–1990 (a) minus and (b) plus standard deviation, and AAIs predicted by simulations in cases (c) B-NDN, (d) B-DDD, (e) B-DGD, (f) B-DGN, and (g) BC-DGD in 1995, all averaged over February to November.

previous section. However, this pattern is also very different from those of the combination sources in the previous section, suggesting the substantial dependence of AAI seasonal patterns to meteorological data and source scheme used in simulations.

6.3. Factors Determining AAI

[48] Before looking closer at the differences due to different wind and mobilization schemes in different regions, it is helpful to look at the seasonal correlations between simulated AAI and their possible determining factors. Along with AAI, Figure 17 also shows seasonal changes of AOD (Figure 17b), dust mobilization (Figure 17c), surface wind speed (at reference height (10 m); Figure 17d), mass weighted average height of dust (Figure 17e), and planetary boundary layer height (PBLH; Figure 17f) (AOD and mobilization for B-NDN84-90 are increased by 26% as are AAIs). PBLH indicates the degree of turbulent mixing and hence affects vertical transport of dust. Table 2 shows correlation coefficients between AAI and these quantities in the Bodele subdomain. Seasonal changes of simulated AAIs generally highly correlate with those of AODs, and mobilizations highly correlate with surface wind speed. However, correlation coefficients of AAIs and AODs with

mobilization and surface wind are not high, especially with GOCART mobilization (i.e., B-DGD and B-DGN). This may be due to greater importance of transport and smaller seasonal change of GOCART mobilization as we shall see in section 6.4. AODs are more highly correlated with mobilization than AAIs in all cases, presumably due to the altitude dependence of the AAI. Similar results are seen for the larger region of the Sahel (not shown).

[49] Contrary to the cases of mobilization and surface wind, AAI correlates well with average dust height with GOCART mobilization and do not with DEAD mobilization, suggesting the greater roles of mobilization in simulations with DEAD and transport in those with GOCART in determining AAIs. Average dust heights highly correlate with PBLH in simulations using NCEP transport but do not in those with DAO transport. Therefore it can be said that PBLH is representative of vertical mixing in NCEP but something other than PBLH is more important in DAO, and as seen in section 6.4, it may be moist convection.

[50] Although seasonality of soil moisture content inversely correlates with mobilization quite well [see *Luo et al.*, 2003, Figure 7], soil moisture does not seem to play an important role in controlling dust mobilization since it does
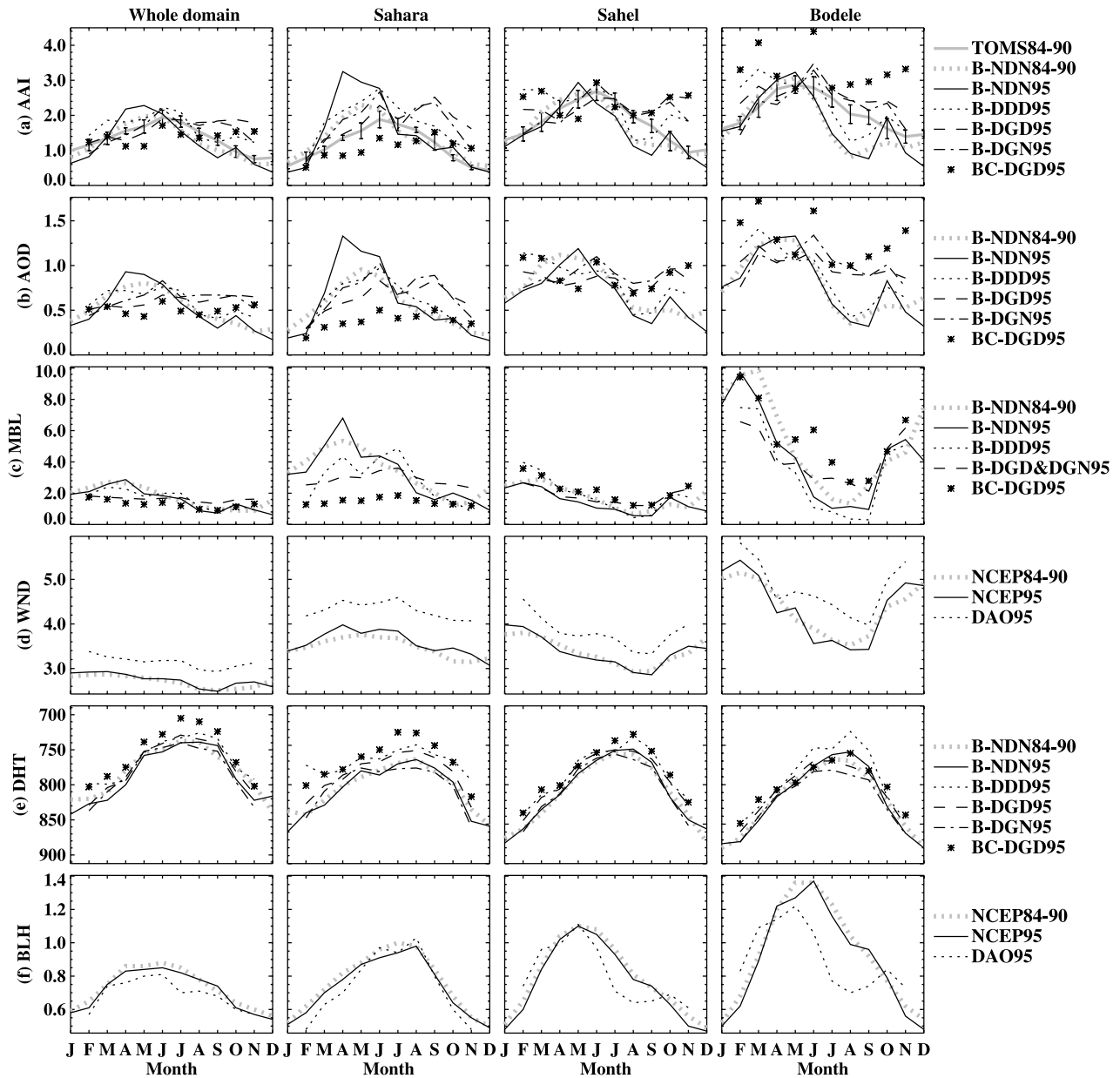
Figure 17. Seasonalities of (a) AAI, (b) AOD, (c) dust mobilization (μg m^{-2} s^{-1}), (d) surface wind speed (m s^{-1}), (e) average height of dust (sigma $\times$ 1000 $\sim$ pressure in hPa), and (f) planetary boundary layer height (km) averaged over the whole domain and Sahara, Sahel, and Bodele subdomains in simulations with different combinations of meteorological data sets and mobilization schemes. For easier comparisons, MS/B-NDN84-90 AAI values in the whole domain are adjusted (26% larger than the original values) so that their annual average equals that of MS/B-NDN95 values. Also, MS/B-NDN84-90 AAI in other subdomains, AOD and mobilization for case B-NDN84-90, and TOMS84-90 AAI are adjusted using the same factor. Error bars for TOMS84-90 show one standard deviation also adjusted with the same factor.

not frequently become high enough to considerably inhibit dust mobilization in Bodele and Sahel in the simulations.

6.4. Explanation of Seasonal Changes of AAI

[51] General qualitative features seen in Figure 17 are summarized in Table 3, in which differences between B-DDD and B-DGD and between B-DGD and B-DGN are organized as differences by mobilization schemes and by meteorological data sets used in transport. Figure 17c shows

that the GOCART scheme (used in B-DGD and B-DGN) produces larger mobilizations in summer and smaller in spring in Sahel and Bodele than DEAD (used in B-NDN and B-DDD) does, so the former cases do not produce the large summertime deficiency in these regions. Since the surface wind minimizes in summer and maximizes in spring in these regions (Figure 17d) (and the amplitude of seasonal change of surface wind speed in DAO is about the same as that of NCEP when normalized), this may be due to a

Table 2. Correlation Coefficients Between Simulated Seasonal Changes of AAI, AOD, Mobilization, Surface Wind Speed, Average Height of Dust, and PBLH Averaged Over Bodele Subdomain[a]

	AAI-AOD	AAI-Mobil	AAI-Wind	AOD-Mobil	Mobil-Wind	AAI-Height	AAI-PBLH	Height-PBLH
NDN84-90	**0.98**	0.33	0.20	0.53	**0.96**	0.11	**0.59**	**0.85**
NDN95	**0.98**	0.24	0.06	0.43	**0.94**	0.14	**0.63**	**0.83**
DDD95	**0.96**	0.48	0.42	**0.68**	0.93	−0.30	**0.85**	−0.12
DGD95	**0.78**	−0.30	−0.15	0.25	**0.97**[b]	0.51	**0.65**	0.08
DGN95	**0.95**	−0.62	−0.51	−0.40	**0.97**[b]	**0.80**	**0.88**	**0.84**

[a]Bold indicates statistical significance of the correlation coefficients with a 95% level.
[b]Same value because DGD and DGN share both mobilization and surface wind.

smaller sensitivity of GOCART mobilization to surface wind speed compared with DEAD mobilization. The smaller sensitivity of GOCART scheme to wind speed is given by *Luo et al.* [2004, Figure 2], which shows that dust mobilization occurs continuously with GOCART while it occurs only in a short time of a day with DEAD and that GOCART produces smaller diurnal and day-to-day variations than DEAD does. This seems due to lower threshold wind speed and less sensitivity to wind speed of GOCART mobilization beyond the threshold, both of which are evident in the instantaneous (not diurnally or monthly averaged) values of surface wind speeds and dust mobilization in the domain in all seasons and all time of a day (not shown).

[52] Since the average height of dust is greater in DAO (B-DGD) than NCEP (B-DGN) transport in all regions and seasons (Figure 17e and Table 3), the vertical mixing is thought to be more efficient in DAO than NCEP simulations, consistent with *Luo et al.* [2003, Figure 10]. This is true even in summer in Bodele and Sahel where the planetary boundary layer height (PBLH) is much lower in DAO than in NCEP (Figure 17f). Since in boreal summer

MATCH predicts more convective precipitation with DAO than NCEP while the resolved vertical advection is stronger with NCEP (not shown), stronger moist convection is considered responsible to the stronger vertical mixing in simulations with DAO transport. B-DGD predicts similar AAI values to B-DGN in summer even though it predicts higher dust height since it predicts lower AOD, which is likely due to differences in horizontal transport and wet deposition. DAO predicts Intertropical Convergence Zone (ITCZ) at the north of Sahel in summer and southerly wind over Sahel, which is less dusty, while NCEP predicts ITCZ just over Sahel and very weak meridional wind component (not shown). B-DGD also predicts more wet deposition following more precipitation in Sahel in summer than B-DGN (not shown).

[53] Although further description of analyses of seasonal changes are not presented here, most of the general features seen in Figure 15 and Table 3 can be explained by weaker sensitivity of GOCART mobilization to the surface wind speed and more efficient vertical mixing with DAO. However, no single combination of mobilization scheme and meteorological data sets used for mobilization and transport

Table 3. Summary of Seasonality of AAI and Its Determining Factors by Meteorological Data Sets for Transport and Mobilization Schemes Used in Simulations[a]

	Sahara			Sahel			Bodele		
	Spring	Summer	Fall	Spring	Summer	Fall	Spring	Summer	Fall
AAI	NDN	DGD	DGD	DDD	DGN	DGD	DDD	DGD	DGD
	>DDD	~DGN	>DGN	>DGD	~DGD	>DGN	>DGD	~DGN	>DGN
	>DGN	>DDD	>DDD	~NDN	>TOMS	>DDD	~NDN	>TOMS	>DDD
	~DGD	>TOMS	>NDN	~TOMS	≫DDD	>NDN	>TOMS	≫DDD	>TOMS
	>TOMS	>NDN	>TOMS	>DGN	>NDN	~TOMS	~DGN	>NDN	>NDN
By schemes[b]	D > G	D < G	D < G	D > G	D ≪ G	D < G	D > G	D ≪ G	D < G
By data sets[c]	N ~ D	N ~ D	N < D	N < D	N ~ D	N < D	N < D	N ~ D	N < D
AOD									
By schemes[b]	D > G	D < G	D < G	D > G	D < G	D < G	D > G	D ≪ G	D < G
By data sets[c]	N > D	N > D	N < D	N ~ D	N > D	N < D	N < D	N > D	N ~ D
Mobilization	strong	strongest	weak	strongest	weak	strong	strongest	weak	strong
By schemes[b]	D > G	D > G	D < G	D > G	D < G	D < G	D > G	D ≪ G	D < G
Surface wind	strong	strongest	weak	strongest	weak	strong	strongest	weak	strong
By data sets[d]	N ~ D	N ~ D	N ~ D	N ~ D	N ~ D	N ~ D	N > D	N < D	N ~ D
Dust height	variable	high	variable	variable	high	variable	variable	high	variable
By data sets[c]	N < D	N < D	N < D	N < D	N < D	N < D	N < D	N < D	N < D
PBLH	variable	high	low	variable	high	low	variable	high	low
By data sets[c]	N > D	N ~ D	N > D	N < D	N > D	N < D	N < D	N ≫ D	N < D

[a]Spring, summer, and fall represent from February to June, from July to September, and October and November, respectively. Symbols refer to generally greater than, much greater than, smaller than, and at similar magnitude as.
[b]D and G refer to DEAD and GOCART schemes, respectively.
[c]Data sets for transport only. N and D refer to NCEP and DAO data sets, respectively.
[d]Comparisons for normalized surface wind speed. The actual values of surface wind are always stronger in DAO than NCEP data set.
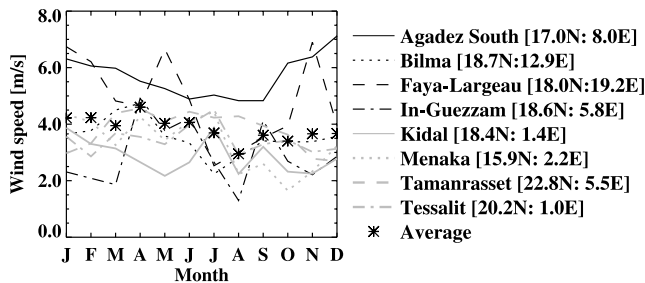
Figure 18. Station data of surface wind speed in northern Sahel averaged over 1994–1999 (derived from NOAA NCDC Daily Station).

can be identified to predict the observed features better than others.

7. Discussion

7.1. Summertime AAI Deficiency in Sahel

[54] *Brooks* [1999] and *Brooks and Legrand* [2000], using their analysis of Infrared Difference Dust Index (IDDI) over 1984–1993, show that dust mobilization becomes highest in the 18–20°N from July to September and sustains high in northern Sahel (15–20°N). The analyses of visibility of *N'Tchayi Mbourou et al.* [1997] also show similar seasonal patterns (although their data indicate number of hours of reduced visibility and are not directly comparable with dust mobilization). These patterns are consistent with TOMS AAI (Figures 5a (right), 14c and 14d), but they are quite different from our simulation results. All simulations including those using GOCART mobilization scheme (B-DGD, B-DGN, and BC-DGD), which do not produce the summertime AAI deficiency, show distinctive minima in mobilization in summer in Sahel and Bodele in response to the minimum mean surface wind in summer. Station data of mean surface wind speed in northern Sahel shown in Figure 18 (derived from NOAA NCDC Daily Station, International Research Institute for Climate Prediction, 2003, available at http://ingrid.ldeo. columbia.edu/SOURCES/.NOAA/.NCDC/.DAILY/. STATION.cuf/, averaged over 1994–1999) also tend to minimize in August and September in this area.

[55] *Brooks* [1999] and *Brooks and Legrand* [2000] state that the dust mobilization in summer in northern Sahel is due to passages of "disturbance lines" or "convective disturbances", which are active near ITCZ. They also state that these disturbances effectively transport dust vertically, which will also contribute to increased AAI values. *Tegen et al.* [2002] points out the discrepancy between their model-predicted dust and the observations are due to underestimate of peak wind speeds in ECMWF used in their model simulations, which is partly due to missing wind gusts in squall lines. *Pye* [1987] also describes the roles of disturbances associated with squall lines in dust mobilization and transport in southern Sahara and Sahel in boreal summer. METEOSAT visible and near infrared images (EUMETSAT, 2005, available at http://www. eumetsat.de/) show that convective clouds are not uncommon over northern Sahel in August and September. *Rowell and Milford* [1993] report that nearly 40% of all squall

lines in the central Sahel (2.5°W–14°E) in August 1985 were observed north of 14°N and over 15% were north of 16°N. On the other hand, MATCH simulations using both NCEP and DAO analyses produce very little cloud water over northern Sahel (column-integrated cloud water amount averaged for 15–20°N is less than for 10–15°N by over (NCEP) or nearly (DAO) one order of magnitude in August and September). Therefore it is suspected that the summertime AAI deficiency in our simulations is caused because these disturbances are not well recreated in our transport simulations. However, although comparisons between maximum and mean wind speeds in the NOAA NCDC station observations and meteorological data sets near the Bodele Depression (15 stations including all in Figure 18 and 66 grid boxes in 12–22°N, 2–20°E) suggest that meteorological data miss the variations of wind speeds significantly (the ratio of maximum to mean wind speeds is less than a half of observations), no evidence is found that they miss maximum wind speeds in summer more than in spring. Direct observations and quantitative analysis are required to determine the reason of summer time deficiency of modeled dust and the possible roles of convective disturbances in dust mobilization and transport.

7.2. Source Evaluation With Uncertainty

[56] In section 5, it is shown that inclusion of new desert (D), cultivation (C), or enhanced Bodele (L) sources in the simulations improves the agreement of the simulated Sahel/Sahara ratio with the observed one. The optimum mixture in terms of the Sahel/Sahara ratio is ~25% of D or C source. However, adding these sources leads to southward bias of the Sahel dust plume and lessens the spatial agreement of AAIs with observation as a whole, although correlation coefficients are usually not statistically distinct from each other (except the case BC over Sahel). Adding sources does not improve the agreements in interannual changes and adds bias to seasonality to a degree of statistical significance in many cases. Assuming the simulated vertical profile is correct, the best mixture in terms of the spatial and temporal correlations is 0–15% of D or C sources. In order for all spatial and temporal correlations of case BD and BC simulations with observation not to be statistically indistinct from case B, D or C source needs to be less than 25% of total dust amount. If we assume that biomass burning obscures our wintertime signal and exclude these months, up to 35% of new desert source or cultivation source are statistically allowed.

[57] However, analyses in section 6 suggest that simulations using different meteorological data sets and mobilization schemes produce quite different patterns. Using DAO data set for mobilization seems to somewhat improve the spatial agreement with observation in the whole domain but slightly deteriorate the correlation within Sahel. Even though mobilization using GOCART scheme does not produce the summertime deficiency, we cannot say GOCART produces better seasonal agreement. Use of a combination source in simulation with GOCART mobilization and DAO data set (case BC-DGD) makes the simulation worse in reproducing the observed seasonality compared to the case with topographic depression source (case B-DGD). The simulated Sahel/Sahara ratio suggests

the optimum mixture is ~20% of cultivation source. The spatial correlations suggest that the simulation best reproduces the observation when cultivation source is 0–15% and the upper bound of cultivation source is 40%. These are very similar to the results of the analysis using NCEP data set and DEAD scheme (i.e., B-NDN versus BC-NDN or BD-NDN) described above.

[58] However, it should be noted that the seasonal pattern produced in case BC-DGD is very different from the case with the same source and different model configuration (case BC-NDN). Therefore it is questionable if we can conclude that the results about source mixture in both model configurations are consistent and therefore likely correct. The large difference in the results from different model configurations suggests a large uncertainty in our results due to uncertainties in the meteorology and source parameterization. As examined in section 4, our calculations of monthly mean observed and simulated AAIs add a certain degree of uncertainty. Biases may be present in other assumed parameters such as simulated vertical profile and optical properties of dust. As seen in section 2, the TOMS observations themselves contain some uncertainties. Comparing simulations for 1995 with 1984–1990 climatology of TOMS AAI also potentially introduces a large bias. These uncertainties combined may surpass the difference in the simulations due to different sources and hence we cannot confidently conclude that the simulation using the optimum mixture of sources derived in previous sections reproduces the observed pattern significantly better than with other sources.

8. Conclusions

[59] In this study, the TOMS Absorbing Aerosol Index (AAI) is simulated for model-predicted dust distributions using radiative transfer calculations. The previously reported properties of AAI; linearity to the aerosol optical depth (AOD) for a given height of dust, quasi-linearity to height of dust for a given AOD, higher AAI for larger particles for a given AOD, are reproduced. Vertical mixing is important in determining AAI, and therefore AAI often maximizes not over the region of maximum source strength but over a downwind region with active vertical mixing, which is unlike the case of AOD.

[60] Using this method, AAI is estimated on the basis of model simulations of North African desert dust and compared with observed TOMS AAI to evaluate the importance of natural and anthropogenic disturbances on land surfaces. The bias in simulated AAI is assumed mainly because of dust source distribution although it may also be due to modeled mobilization, atmospheric transport and assumed optical properties of dust. The base case simulations are conducted using MATCH transport model and DEAD dust mobilization scheme driven by NCEP reanalysis data. AAIs are calculated for monthly averaged diurnal mean dust, atmosphere, solar geometry and fixed satellite position at nadir. These simplification may lead to an error up to about 1 AAI unit when combined compared to calculations under more realistic conditions, and a large error usually occurs over the region of high AAI (dust loading). Change in the assumed particle size distribution has a large effect on the values of simulated AAI. In our sensitivity study where

mass fractions of dust particles are reduced in smaller sizes and increased in larger sizes, the AAI as well as AOD values become about a half of those with original size distribution. Changing the size distribution did not, however, change the spatial or temporal distribution of the simulated distribution. Although these errors introduce an important uncertainty in comparisons of observed and simulated AAIs, they are not as large as the model observational errors seen in the analysis, or uncertainties due to changing the model formulation.

[61] The simulations are conducted for topographic depression source, and three additional sources: new desert, cultivation, and enhanced Bodele sources. The spatial distributions of simulated AAI using topographic depression source capture the observed features generally well. However, annual mean distribution overestimates AAI over Sahara and underestimates over Sahel. The simulation using a topographic depression source overestimates AAI in spring over Sahara and significantly underestimates in summer over Sahel and Bodele Depression. It also fails to capture the interannual changes of AAI. Adding the new desert source or the cultivation source, or enhancing the Bodele Depression source improves the annual mean Sahel/Sahara ratios, but leads to further overestimate of AAI in spring and does not improve the large underestimates in summer. Adding other sources does not improve the agreement of interannual changes either and makes the AAI distributions in Sahel biased to the south. The addition of the new desert source or the cultivation source makes the resulting spatial and temporal correlations with observations statistically significantly lower compared to the case with topographic depression source only. The optimum mixing of new desert or cultivation sources is estimated to be 25% in terms of Sahel/Sahara ratio and 0–15% in terms of spatial and temporal correlations with observation. Dust from these sources needs to be less than 25–35% of total dust loading in order to keep them statistically indistinguishable.

[62] The sensitivity studies are performed using DAO meteorology and GOCART mobilization scheme. Simulations using different meteorological data sets and mobilization schemes produce very different spatial and temporal distributions of AAI. These differences are explained by assuming smaller wind speed dependence of GOCART mobilization and more efficient vertical mixing with transport using DAO. The large underestimates of AAI in summer in Sahel and Bodele are suspected to be due to missing subgrid-scale disturbances in model simulations. The simulation using DAO meteorology and GOCART mobilization scheme for a combination source may be interpreted in a qualitatively similar way to the base case simulations; the addition of cultivation source makes the simulation worse in terms of reproducing observed AAI patterns, the optimum mixture of cultivation source is 20% in terms of Sahel/Sahara ratio and 0–15% in terms of spatial correlations, and it needs to be less than 40% to be statistically indistinct from the optimum mixture. However, these propositions about different source types may not be able to be conclusive due to the large uncertainties in simulations using meteorological data sets and source parameterizations as well as in observed data. More intensive analysis with other data sets is required to assess

the relative roles of natural topographic depressions and surface disturbances in dust generation.

References

Belly, P. Y. (1964), Sand movement by wind, *U.S. Army Coastal Eng. Res. Tech. Memo. 1*, 38 pp.

Brooks, N. (1999), Dust-climate interactions in the Sahel-Sahara zone of northern Africa, with particular reference to late twentieth century Sahelian drought, Ph.D. thesis, Clim. Res. Unit, Univ. of East Anglia, Norwich, UK.

Brooks, N., and M. Legrand (2000), Dust variability over northern Africa and rainfall in the Sahel, in *Linking Climate Change to Land Surface Change*, edited by S. McLaren and D. Kniveton, pp. 1–25, Springer, New York.

Cakmur, R. V., R. L. Miller, and I. Tegen (2001), A comparison of seasonal and interannual variability of soil dust over the Atlantic Ocean as inferred by the TOMS AI and AVHRR AOT retrievals, *J. Geophys. Res.*, *106*, 18,287–18,303.

Chadwick, O. A., L. A. Derry, P. M. Vitousek, B. J. Huebert, and L. O. Hedin (1999), Changing sources of nutrients during four million years of ecosystem development, *Nature*, *397*, 491–496.

Colarco, P. R., O. B. Toon, O. Torres, and P. J. Rasch (2002), Determining the UV imaginary index of refraction of Saharan dust particles from Total Ozone Mapping Spectrometer data using a three-dimensional model of dust transport, *J. Geophys. Res.*, *107*(D16), 4289, doi:10.1029/2001JD000903.

Colarco, P. R., O. B. Toon, and B. N. Holben (2003), Saharan dust transport to the Caribbean during PRIDE: 1. Influence of dust sources and removal mechanisms on the timing and magnitude of downwind aerosol optical depth events from simulations of in situ and remote sensing observations, *J. Geophys. Res.*, *108*(D19), 8589, doi:10.1029/2002JD002658.

Dai, A., I. Y. Fung, and A. D. D. Genio (1996), Surface observed global land precipitation variations during 1900–88, *J. Clim.*, *10*, 2943–2962.

Dave, J. V. (1978), Effect of aerosols on the estimation of total ozone in an atmospheric column from the measurements of its ultraviolet radiance, *J. Amos. Sci.*, *35*, 899–911.

Fecan, F., B. Marticorena, and G. Bergametti (1999), Parameterization of the increase of the Aeolian erosion threshold wind friction velocity due to soil moisture for arid and semi-arid area, *Ann. Geophys.*, *17*, 149–157.

Gillette, D. A., and R. Passi (1988), Modeling dust emission caused by wind erosion, *J. Geophys. Res.*, *93*, 14,233–14,242.

Ginoux, P., and O. Torres (2003), Empirical TOMS index for dust aerosol: Applications to model validation and source characterization, *J. Geophys. Res.*, *108*(D17), 4534, doi:10.1029/2003JD003470.

Ginoux, P., M. Chin, I. Tegen, J. M. Prospero, B. Holben, O. Dubovik, and S. J. Lin (2001), Sources and distributions of dust aerosols simulated with the GOCART model, *J. Geophys. Res.*, *106*, 20,255–20,273.

Ginoux, P., J. M. Prospero, O. Torres, and M. Chin (2004), Long-term simulation of global dust distribution with the GOCART model: correlation with North Atlantic Oscillation, *Environ. Modell. Software*, *19*, 113–128.

Goudie, A. S., and N. J. Middleton (2001), Saharan dust storms: Nature and consequences, *Earth Sci. Rev.*, *56*(1–4), 179–204.

Grini, A., and C. S. Zender (2004), Roles of saltation, sandblasting, and wind speed variability on mineral dust aerosol size distribution during the Puerto Rican Dust Experiment (PRIDE), *J. Geophys. Res.*, *109*, D07202, doi:10.1029/2003JD004233.

Haxeltine, A., and I. C. Prentice (1996), BIOME3: An equilibrium terrestrial biosphere model based on ecophysiological constraints, resource availability, and competition among plant functional types, *Global Biogeochem. Cycles*, *10*, 693–709.

Herman, J. R., P. K. Bhartia, O. Torres, C. Hsu, C. Seftor, and E. Celarier (1997), Global Distribution of UV-absorbing aerosols from Nimbus-7/TOMS data, *J. Geophys. Res.*, *102*, 16,911–16,922.

Hsu, N. C., J. R. Herman, O. Torres, B. N. Holben, D. Tanre, T. F. Eck, A. Smirnov, B. Chatenet, and F. Lavenu (1999), Comparisons of the

TOMS aerosol index with sun-photometer aerosol optical thickness: Results and applications, *J. Geophys. Res.*, *104*(D6), 6269–6279.

Intergovernmental Panel on Climate Change (IPCC) (2001), *Climate Change 2001: The Scientific Basis: Contribution of Working Group I to the Third Assessment Report of the Intergovernmental Panel on Climate Change*, 881 pp., Cambridge Univ. Press, New York.

Iversen, J. D., and B. R. White (1982), Saltation threshold on Earth, Mars and Venus, *Sedimentology*, *29*, 111–119.

Kalnay, E., et al. (1996), The NCEP/NCAR 4-year reanalysis Project, *Bull. Am. Meteorol. Soc.*, *77*(3), 437–471.

Kistler, R., et al. (2001), The NCEP-NCAR 50-year reanalysis: Monthly means CD-ROM and documentation, *Bull. Am. Meteorol. Soc.*, *82*(2), 247–267.

Luo, C., N. M. Mahowald, and J. del Corral (2003), Sensitivity study of meteorological parameters on mineral aerosol mobilization, transport, and distribution, *J. Geophys. Res.*, *108*(D15), 4447, doi:10.1029/2003JD003483.

Luo, C., N. Mahowald, and C. Jones (2004), Temporal variability of dust mobilization and concentration in source regions, *J. Geophys. Res.*, *109*, D20202, doi:10.1029/2004JD004861.

Mahowald, N. M., and J. Dufresne (2004), Sensitivity of TOMS aerosol index to boundary layer height: Implications for detection of mineral aerosol sources, *Geophys. Res. Lett.*, *31*, L03103, doi:10.1029/2003GL018865.

Mahowald, N. M., and L. M. Kiehl (2003), Mineral aerosol and cloud interactions, *Geophys. Res. Lett.*, *30*(9), 1475, doi:10.1029/2002GL016762.

Mahowald, N. M., P. J. Rasch, B. E. Eaton, S. Whittleston, and R. G. Prinn (1997), Transport of 222 radon to the remote troposphere using MATCH and assimilated winds from ECMWF and NCEP/NCAR, *J. Geophys. Res.*, *102*(D23), 28,139–28,151.

Mahowald, N. M., C. S. Zender, C. Luo, D. Savoie, O. Torres, and J. del Corral (2002), Understanding the 30-year Barbados desert dust record, *J. Geophys. Res.*, *107*(D21), 4561, doi:10.1029/2002JD002097.

Mahowald, N. M., C. Luo, J. del Corral, and C. S. Zender (2003), Interannual variability in atmospheric mineral aerosols from a 22-year model simulation and observational data, *J. Geophys. Res.*, *108*(D12), 4352, doi:10.1029/2002JD002821.

Mahowald, N. M., G. D. R. Rivera, and C. Luo (2004), Comment on "Relative importance of climate and land use in determining present and future global soil dust emission" by I. Tegen et al., *Geophys. Res. Lett.*, *31*, L24105, doi:10.1029/2004GL021272.

Marticorena, B., and G. Bergametti (1995), Modeling the atmospheric dust cycle: 1. Design of a soil-derived dust emission scheme, *J. Geophys. Res.*, *100*(D8), 16,415–16,430.

Martin, J. H. (1990), Glacial-interglacial CO_2 change: The iron hypothesis, *Paleoceanography*, *5*(1), 1–13.

Matthews, E. (1983), Global vegetation and land use: New high-resolution data bases for climate studies, *J. Clim. Appl. Meteorol.*, *22*, 474–487.

Menaout, J.-C., L. Abbadie, F. Lavenu, P. Loudjani, and A. Podaire (1991), Biomass burning in West African savannas, in *Global Biomass Burning*, edited by. J. S. Levine, pp. 133–142, MIT Press, Cambridge, Mass.

Miller, R. L., and I. Tegen (1998), Climate response to soil dust aerosols, *J. Clim.*, *11*, 3247–3267.

N'Tchayi Mbourou, G., J. J. Bertrand, and S. E. Nicholson (1997), The diurnal and seasonal cycles of wind-borne dust over Africa north of the equator, *J. Appl. Meteorol.*, *36*, 868–882.

Pierluissi, J. H., and G.-S. Peng (1985), New molecular transmission band models for LOWTRAN, *Opt. Eng.*, *24*(3), 541–547.

Prospero, J. M., and R. T. Nees (1986), Impact of the North African drought and El Nino on mineral dust in the Barbados trade winds, *Nature*, *320*, 735–738.

Prospero, J. M., P. Ginoux, O. Torres, S. E. Nicholson, and T. E. Gill (2002), Environmental characterization of global sources of atmospheric soil dust identified with the Nimbus 7 Total Ozone Mapping Spectrometer (TOMS) absorbing aerosol product, *Rev. Geophys.*, *40*(1), 1002, doi:10.1029/2000RG000095.

Pye, K. (1987), *Aeolian Dust and Dust Deposits*, 334 pp., Springer, New York.

Rasch, P. J., N. M. Mahowald, and B. E. Eaton (1997), Representation of transport, convection and hydrologic cycle in chemical transport models: Implications for the modeling of short-lived and soluble species, *J. Geophys. Res.*, *102*(D23), 18,127–18,138.

Ricchiazzi, P., et al. (1998), SBDART: A research and teaching software tool for plane-parallel radiative transfer in the Earth's atmosphere, *Bull. Am. Meteorol. Soc.*, *79*(10), 2101–2114.

Rowell, D. P., and J. R. Milford (1993), On the generation of African squall lines, *J. Clim.*, *6*, 1181–1193.

Saxton, K., D. Chandler, L. Stetler, B. Lamb, C. Claiborn, and B. H. Lee (2000), Wind erosion and fugitive dust fluxes on agricultural lands in the Pacific northwest, *Trans. ASAE*, *43*, 623–630.

Sinyuk, A., O. Torres, and O. Dubovik (2003), Combined use of satellite and surface observations to infer the imaginary part of refractive index of Saharan dust, *Geophys. Res. Lett.*, *30*(2), 1081, doi:10.1029/2002GL016189.

Stamnes, K., S. Tsay, W. Wiscombe, and K. Jayaweera (1988), Numerically stable algorithm for discrete-ordinate-method radiative transfer in multiple scattering and emitting layered media, *Appl. Opt.*, *27*, 2502–2509.

Stroppiana, D., P. A. Brivio, and J.-M. Gréoire (2000), Modelling the impact of vegetation fires, detected from NOAA-AVHRR data, on tropospheric chemistry in tropical Africa, in *Biomass Burning and Its Interrelationships With the Climate System*, edited by J. L. Innes, M. Beniston, and M. M. Verstraete, pp. 193–213, Springer, New York.

Tegen, I., and I. Fung (1994), Modeling of mineral dust in the atmosphere: Sources, transport, and optical thickness, *J. Geophys. Res.*, *99*, 22,897–22,914.

Tegen, I., and I. Fung (1995), Contribution to the atmospheric mineral aerosol load from land surface modification, *J. Geophys. Res.*, *100*(D9), 18,707–18,726.

Tegen, I., S. P. Harrison, K. Kohfeld, I. C. Prentice, M. Coe, and M. Heimann (2002), Impact of vegetation and preferential source areas on global dust aerosol: Results from a model study, *J. Geophys. Res.*, *107*(D21), 4576, doi:10.1029/2001JD000963.

Tegen, I., M. Werner, S. P. Harrison, and K. E. Kohfeld (2004), Relative importance of climate and land use in determining present and future global soil dust emission, *Geophys. Res. Lett.*, *31*, L05105, doi:10.1029/2003GL019216.

Torres, O., P. K. Bhartia, J. R. Herman, Z. Ahmad, and J. Gleason (1998), Derivation of aerosol properties from satellite measurements of backscattered ultraviolet radiation: Theoretical basis, *J. Geophys. Res.*, *103*, 17,099–17,110.

Torres, O., P. K. Bhartia, J. R. Herman, A. Sinyuk, P. Ginoux, and B. Holbren (2002), A long-term record of aerosol optical depth from TOMS observations and comparison to AERONET measurements, *J. Atmos. Sci.*, *59*, 398–413.

White, B. R. (1979), Soil transport by winds on Mars, *J. Geophys. Res.*, *84*, 4643–4651.

Zender, C. S., D. Newman, and O. Torres (2003a), Spatial heterogeneity in aeolian erodibility: Uniform, topographic, geomorphic, and hydrologic hypotheses, *J. Geophys. Res.*, *108*(D17), 4543, doi:10.1029/2002JD003039.

Zender, C. S., H. Bian, and D. Newman (2003b), Mineral Dust Entrainment and Deposition (DEAD) model: Description and 1990s dust climatology, *J. Geophys. Res.*, *108*(D14), 4416, doi:10.1029/2002JD002775.

———————————

J.-L. Dufresne, Laboratoire de Meteorologie Dynamique, CNRS, Institut Pierre Simon Laplace, Universite Paris 6, Boite 99, F-75252 Paris Cedex 05, France.

C. Luo, Earth System Science, University of California, Irvine, CA 92697, USA. (cluo@uci.edu)

N. Mahowald and M. Yoshioka, Climate and Global Dynamics Division, NCAR, P.O. Box 3000, Boulder, CO 80305, USA. (mahowald@ucar.edu; yoshioka@ucar.edu)